Satchithananthan, U. *et al*. (2021). *Géotechnique* **71**, No. 10, 893–910 [https://doi.org/10.1680/jgeot.19.P.244]

Axial sliding resistance of partially embedded offshore pipelines

UMASHANKARAN SATCHITHANANTHAN*, SHAH NEYAMAT ULLAH†, FOOK-HOU LEE‡ and HAI GU§

This paper presents the results of centrifuge model tests and three-dimensional large-deformation finite-element analysis on axial pipe–soil sliding behaviour of partially embedded subsea pipelines. A three-dimensional re-meshing and interpolation technique with small strain approach was adopted using the Abaqus mesh-to-mesh solution mapping feature with the Cam Clay model. The parameters studied include soil properties, interface friction coefficient, embedment depth and post-lay reduction in vertical load. Embedment depth and post-lay load reduction were found to exercise the strongest influence on the post-consolidation and sliding behaviour. Empirical relationships correlating centrifuge experiments and numerical modelling are proposed for the embedment enhancement factor in terms of the embedment and vertical load ratios, under conditions of very slow sliding, corresponding to the drained condition. For very fast sliding, corresponding to effectively undrained conditions, similar relationships involving embedment and vertical load ratios and interface friction coefficients are also proposed. Finally, the variation of embedment enhancement factor with sliding velocity is expressed in terms of a relative enhancement index, Ψ, which can be adequately described by hyperbolic relationships for the complete range of consolidation history. These relationships provide a basis for the evaluation of the embedment enhancement factor corresponding to an arbitrary sliding velocity, which can be used in routine analysis and design of as-laid underwater pipelines in soft clayey soils.

KEYWORDS: centrifuge modelling; clays; numerical modelling; offshore engineering; pipes & pipelines; soil/structure interaction

INTRODUCTION

Offshore deep-water pipelines for petroleum and hydrocarbon transport are often subjected to pressure and temperature cycles arising from start-ups and shutdowns, which give rise to pipeline expansion and contraction. Successive cycles of expansion and contraction may cause the pipeline to displace longitudinally, a phenomenon known as 'axial walking' (Carr *et al*., 2008; Ballard *et al*., 2013). Pipeline expansion and subsequent mobilisation of the pipe–soil interface friction along segments of the pipeline may also cause a build-up of compressive stress along the pipe, which may result in lateral buckling of the pipeline (Bruton *et al*., 2008).

Current design guidelines for axial pipe–soil sliding resistance are largely empirical. The DNVGL-RP-F114 (DNV GL, 2017) guideline provides empirical equations for estimating the axial pipe–soil friction for fully drained and undrained situations. BS 8010-3 (BSI, 1993) suggests an effective friction coefficient between 0·3 and 1·0, based on North Sea experience. However, axial pipe–soil resistance between the drained and undrained extremes remains largely unknown, and design guidelines are still unavailable.

Whereas shallow water pipelines are usually buried in pre-dug trenches, deep-water pipelines are often simply laid on the seabed. As a result, the pipe is only partially embedded, typically to roughly half the pipe diameter, into the seabed. In such situations, the lateral earth pressure on both sides of the partially embedded pipe arising from soil heave during the embedment process also contributes to the pipe–soil sliding resistance. Hence, axial pipe–soil resistance is often higher than that obtained by just multiplying the submerged pipe weight by a pipe–soil interface friction coefficient (Satchithananthan *et al*., 2019). White & Randolph (2007) proposed that the enhancement to the axial pipe–soil resistance due to pipe embedment could be represented by a contact enhancement factor, which is a function of pipe embedment depth. However, their method of estimating the enhancement factor assumed a uniform contact stress distribution around the pipe circumference and an elastic soil, which is unrealistic. Using numerical analyses to simulate pipe touch-down on the seabed, Ansari *et al*. (2014) proposed an alternative expression for the enhancement factor to account for the non-uniform stress distribution around the pipe circumference. However, in their study, the pipe touch-down and sliding analyses were decoupled. The touch-down analyses were two-dimensional plane strain whereas the sliding analyses were three-dimensional (3D). In the sliding analyses, the pipe was modelled as wished in place (WIP).

Randolph *et al*. (2012) and Ansari *et al*. (2014) examined the effect of pipe displacement rate on the axial pipe–soil resistance using finite-element analyses with the Cam Clay model. However, both assumed the pipe to be WIP (i.e. pre-embedded), which does not model the stress or the excess pore pressures due to pipe penetration. Boukpeti &

Manuscript received 24 August 2019; revised manuscript accepted 26 June 2020. Published online ahead of print 31 July 2020.
Discussion on this paper closes on 1 February 2022, for further details see p. ii.
*Department of Civil & Environmental Engineering, National University of Singapore, Singapore (Orcid:0000-0001-8345-0821).
†School of Engineering and Technology, Gladstone Engineering Centre, Central Queensland University, Gladstone, Queensland, Australia.
‡Department of Civil & Environmental Engineering, National University of Singapore, Singapore (Orcid:0000-0001-6755-3951).
§ American Bureau of Shipping Corporate Technology, Houston, TX, USA.

White (2017) reported interface shear box tests on axial pipe–soil resistance. However, the interface shear box apparatus does not model the curved pipe–soil interface, or the stresses induced by soil heave during embedment. Furthermore, during the pipe-laying process, the pipe may over-penetrate beyond its self-weight-induced depth (Palmer, 2008; Randolph & White, 2008; Westgate *et al.*, 2012). The subsequent post-penetration reduction in vertical load will alter the stress state of the soil around the pipe in ways that remain unclear and cannot be modelled by WIP analyses or by interface tests in a direct shear box.

This paper examines the effects of initial embedment depth, post-penetration reduction in pipe vertical load and post-lay consolidation of soil beneath the pipe before sliding episodes, and pipe–soil contact friction on sliding resistance, using centrifuge model tests and 3D effective stress large-deformation finite-element (LDFE) analyses. The re-meshing and interpolation technique with small strain (RITSS) approach was adopted to account for the large mesh distortions caused by pipe penetration. Centrifuge model test data were used to verify and complement the numerical results. Based on the results, equations are proposed to predict the undrained, partially and fully drained axial pipe–soil resistance.

CENTRIFUGE MODEL TEST

The experimental set-up of the centrifuge model tests has been reported in Satchithananthan *et al.* (2019). Hence, only a brief summary is presented herein. The centrifuge tests were carried out under 10***g*** model gravity (where ***g*** is Earth's gravitational acceleration). As Fig. 1 shows, the experimental set-up for modelling pipe penetration and sliding consisted of a servo-motor actuating system driving a sliding table. The model pipe was underslung beneath the sliding table by way of a hydraulic cylinder, which applied the desired vertical displacement or load on the pipe. The stainless steel model pipe had a segmental construction, comprising a long central test section placed between two dummy sections of the same outer diameter of 80 mm. The function of the two dummy sections is to eliminate end effects on the test pipe section. The drained friction coefficient of the stainless steel–clay interface was measured to be ~0·3 from interface shear box tests (Satchithananthan *et al.*, 2019). Satchithananthan *et al.* (2019) reported only results corresponding to a prototype pipe diameter D_p of 0·35 m at an embedment depth of 0·5D_p. This paper includes results for a bigger pipe having a prototype diameter D_p of 0·8 m at embedment depths of 0·3D_p, 0·5D_p and 0·7D_p.

The model clay bed was prepared from kaolin clay powder, the properties of which are shown in Table 1. The model clay bed was first consolidated under 1***g*** conditions with 1 kPa surcharge for 7 days, after which it was transferred to the centrifuge and further consolidated under 10***g***. The resulting clay bed is normally consolidated throughout its depth, except for the top ~1·5 cm near the ground surface, which is overconsolidated. The undrained strength of the clay was measured using a T-bar, with the shallow-depth strength corrections procedure by White *et al.* (2010). After the model clay bed had been equilibrated under 10***g*** gravity, the model pipe was penetrated to the desired embedment depth with a velocity v_e of 1 mm/s. This corresponds to a dimensionless velocity $v_e D_p/c_v$ of approximately 60, which is fast enough to ensure undrained penetration (Finnie & Randolph, 1994; Randolph & Hope, 2004; Chung *et al.*, 2006). After penetration to the prescribed depth, the vertical load on the pipe was maintained at its final penetration resistance. Lay-induced excess pore pressures were allowed to dissipate fully prior to several episodes of axial pipe sliding with different velocities.

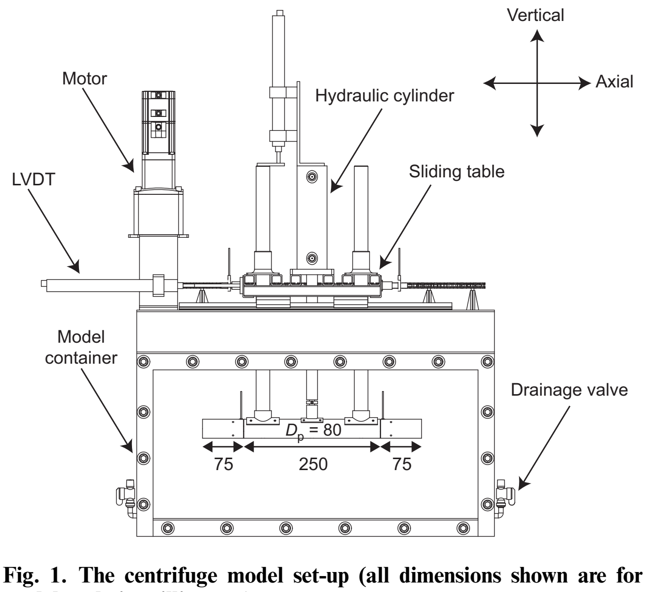

Fig. 1. The centrifuge model set-up (all dimensions shown are for model scale in millimetres)

NUMERICAL ANALYSIS

Finite-element model

The pipe embedment, consolidation and axial sliding events were analysed using 3D coupled-consolidation RITSS analysis implemented in Abaqus (2016). Soil flow due to the pipe penetration was analysed using the RITSS algorithm of Ullah *et al.* (2018), which was based on the approach by Hu & Randolph (1998a, 1998b). The half-pipe was modelled as a rigid body using four-noded rigid shell elements, with the pipe ends protruding beyond the soil boundaries to eliminate end effects (see Fig. 2). The soil domain was modelled as a quarter-space and discretised into eight-noded linear brick elements with coupled pore pressure–displacement degrees of freedom (element type C3D8P). The mesh sensitivity was studied; the soil element size close to the pipe circumference was varied between 0·006D_p and 0·12D_p, while the far boundary element sizes were maintained at 0·75D_p. Based on the pipe penetration resistance response, a soil element size of 0·03D_p was selected close to the pipe circumference, which was sufficient for a good balance between accuracy and computational time. The pipe–soil interface was modelled using Coulomb's frictional contact with the prescribed friction coefficient. In most of the cases, the friction coefficient used was 0·3, but parametric studies were also conducted using friction coefficients of 0·1 and 0·42 to assess the effect of contact friction.

Table 1. Physical properties of Malaysian kaolin clay (Goh, 2003)

Property	Value
Liquid limit, W_L	79·8%
Plastic limit, W_p	35·1%
Specific gravity, G_s	2·6 kN/m^3
Bulk unit weight, γ_{bulk}	16·39 kN/m^3
Permeability, k	2·0 × 10^{-8} m/s
Coefficient of consolidation, c_v	40 m^2/year
Critical state angle of friction	23°
Slope of critical state line, M	0·9
Slope of normal compression line, λ	0·25
Slope of unloading/reloading line, κ	0·05

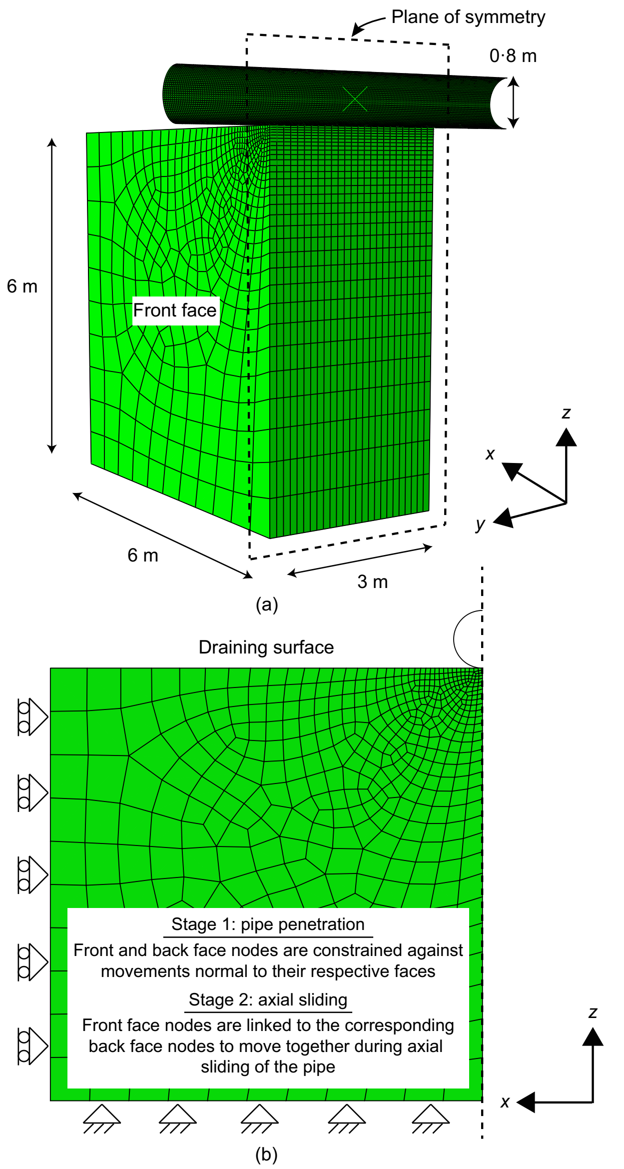

Fig. 2. The initial finite-element model; (a) model dimensions and (b) boundary conditions

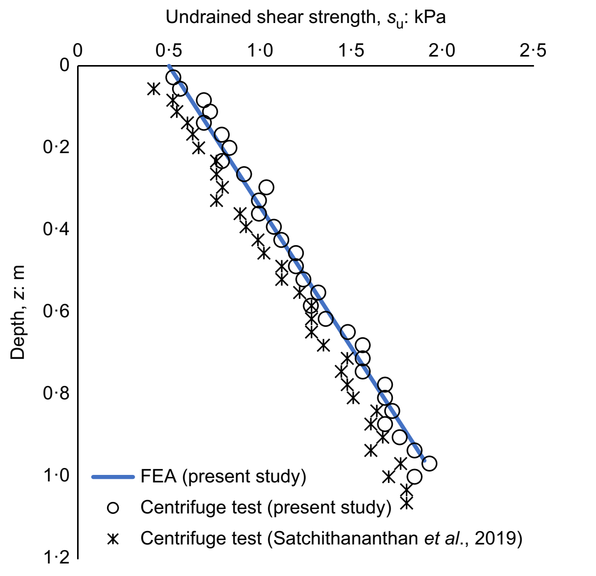

Fig. 3. The undrained soil strength profile (with corrections at shallow depth by the procedure of White *et al.* (2010)). Experimental values were measured using a T-bar

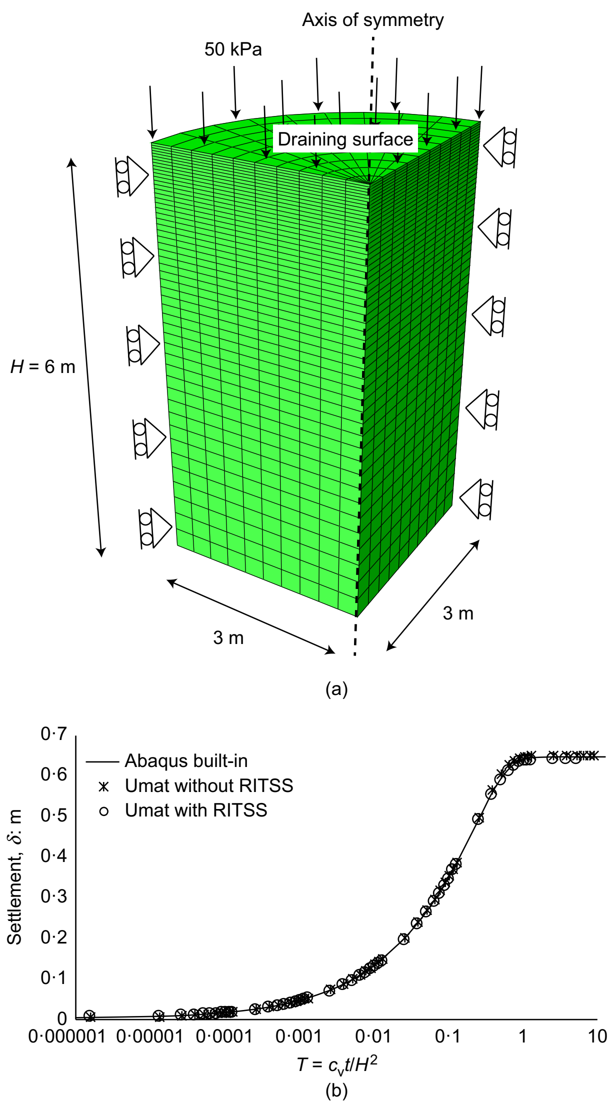

Fig. 4. One-dimensional consolidation analysis: (a) finite-element model, loading and boundary conditions; (b) settlement response

Table 2. Parameters for Cam Clay model

Parameter	Value
Slope of normal compression line, λ	0·25
Slope of unloading/reloading line, κ	0·05
Void ratio at $p' = 1$ kPa on virgin compression line, e_N	2·2
Slope of critical state line, M	0·9
Poisson's ratio, v'	0·3
Coefficient of lateral earth pressure, K_0	0·6
Dry unit weight, γ_{dry}	6 kN/m^3

Following Yi *et al.* (2014) and Li *et al.* (2017), the Cam Clay model, with the parameters shown in Table 2, was used to model the clay bed. As shown in Fig. 2(b), the soil surface was modelled as an open drainage boundary with zero excess pore pressure. The bottom of the soil domain was constrained against all movements. A small distributed load of ~2 kPa was applied on the soil surface to ensure that the undrained shear strength profile was consistent with that in the centrifuge tests. As Fig. 3 shows, the measured undrained shear strength at the soil surface, from Satchithananthan *et al*. (2019) and the current centrifuge tests, is non-zero; this arises from the overconsolidated state caused by the 1***g*** surcharge of 1 kPa. On the other hand, the Cam Clay model would have no strength and infinite void ratio when the effective stress is zero, even in an overconsolidated state. Hence, a small non-zero effective stress is also necessary to match the strength profile and ensure numerical stability.

Implementation of RITSS with Cam Clay soil model

The RITSS approach involves a series of small-strain finite-element analyses, interspersed with re-meshing and solution mapping operations to avoid excessive element distortion (Hu & Randolph, 1998a). The procedure used herein is based on the Ullah *et al*. (2018) implementation, which utilises the Abaqus mesh-to-mesh solution mapping feature, thereby obviating intermediate user coding for mapping solutions and updating initial conditions for continuation of analysis. The Abaqus mesh-to-mesh solution mapping operates by interpolating results from nodes in the old mesh to either nodes or integration points in the new mesh. The first step involves associating solution variables with nodes in the old mesh. For nodal solution variables, such as nodal temperature or pore pressure, this association is automatic. For integration point variables, Abaqus obtains the solution at the nodes by extrapolating values from

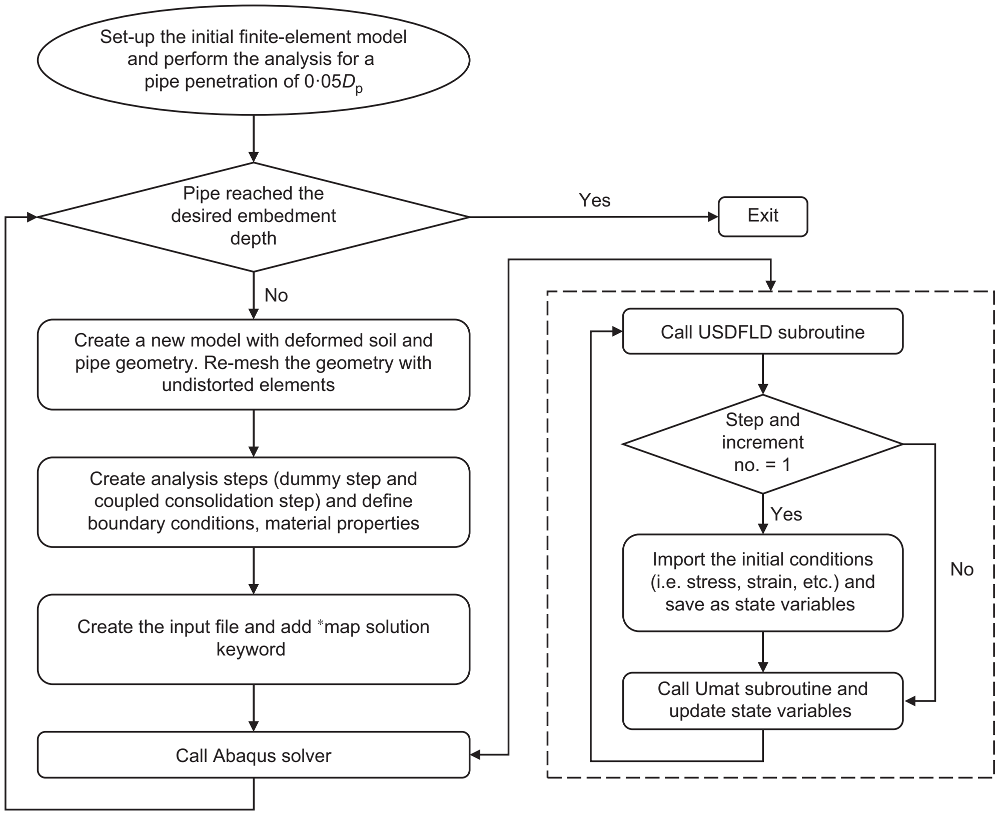

Fig. 5. The overall scheme of RITSS procedure

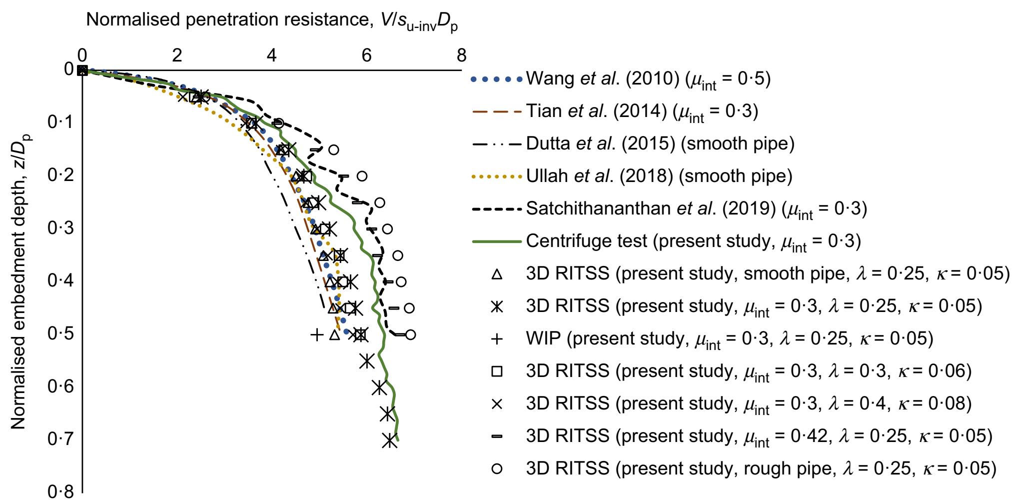

Fig. 6. The pipe penetration response; $s_{u\text{-inv}}$ is the undrained strength at the pipe invert, and D_p is the pipe diameter

integration points to the nodes in the same element and then averaging these values over all similar elements abutting each node. Finally, the solution variables from the old element nodes are interpolated to the integration points and nodes of the new model (Abaqus, 2016).

However, preliminary trials showed that Abaqus is unable to transfer the size of the current yield surface from the old to the new mesh for its built-in Cam Clay model. Hence, the Cam Clay model was coded into a user-defined material subroutine Umat. The Umat routine adopted a return mapping approach, termed the 'cutting plane algorithm', with path-dependent strategy as the Cam Clay stress update algorithm (Huang & Griffiths, 2009). The yield surface size was stored and updated as a state variable inside Umat. After the solution had been mapped from the previous mesh, the updated yield surface size, as well as the integration point variables, such as stresses, strains, void ratio and pore pressures, for the new mesh were accessed through the Abaqus utility routine GETVRM in conjunction with the user-defined field subroutine USDFLD. These were then passed back into Umat as state variables. Fig. 4(a) shows the finite-element model, loading and boundary conditions for a one-dimensional consolidation analysis conducted to verify the Umat subroutine. As Fig. 4(b) shows, an almost identical settlement response was observed for the Abaqus built-in Cam Clay model, Umat without RITSS and Umat with RITSS.

Three-dimensional RITSS analysis procedure

Figure 5 shows the overall scheme of the RITSS procedure with the Cam Clay model. Geostatic equilibrium of the soil under its own self-weight was first established. The pipe was then penetrated into the soil to a depth of 0·05 times the pipe diameter D_p over 1 s. The time duration of the pipe penetration was kept short to simulate an effectively undrained condition. During this stage, the two faces of the mesh intersected by the pipe section were constrained against movements normal to their respective faces. The deformed geometry of the pipe and soil was then imported into a new model and re-meshed with undistorted elements using the procedure of Ullah *et al.* (2018). The solutions from the previous analysis were then transferred to the new mesh by the Abaqus mesh-to-mesh solution mapping feature. The process was then repeated, with the geostatic step being replaced by an equilibrium step without any load increment, to equilibrate any residual out-of-balance stresses arising from the mapping algorithm. The penetration was then repeated for a further depth increment of $0{\cdot}05D_p$. This sequence of steps was repeated until the desired pipe embedment depth was reached (Fig. 5).

After the desired embedment depth was reached, a vertical load was applied on the pipe to simulate the pipe weight, while allowing the pipe to move freely in the vertical direction. This was achieved over a short period of time allowing no excess pore pressure dissipation, maintaining essentially an undrained condition. The pipe weight V' was set to be equal to or less than the computed penetration resistance V at the final embedment depth. The latter is done to investigate the effect of reduction in vertical load after pipe laying due to operational conditions (e.g. Palmer, 2008). The ratio V'/V will hereafter be termed the 'vertical load ratio' (VLR). The scenario that subsequent operational pipe weight may exceed the computed penetration resistance during touch-down is not considered herein. The laying-induced excess pore pressures were then allowed to dissipate fully prior to axial sliding.

The sliding of the pipe was then modelled by displacing the pipe axially over a distance of one pipe diameter. During axial sliding RITSS re-mapping is not required since pipe sliding does not involve large mesh distortions. During this stage, the two faces of the mesh intersected by the pipe section are allowed to move, but the nodes are tied so that nodes with the same (x, z) coordinates undergo the same displacement; this being achieved using a 'tied boundary' condition (Fig. 2(b)). This simulates an infinitely long pipe shearing an infinite extent of ground in the longitudinal direction. The axial sliding analysis was carried out for different dimensionless velocities v_sD_p/c_v, from 1500 to 0·0097, to model conditions ranging from undrained to drained, respectively. The coefficient of consolidation c_v was estimated from the coefficient of volume change m_v at the initial pipe invert location. For normally consolidated Cam Clay, this was estimated as

$$c_v = \frac{k}{m_v\gamma_w},\ m_v = \frac{\lambda}{(1+e_0)\sigma'_v} \tag{1}$$

where σ'_v is the vertical effective stress; e_0 is the initial void ratio; k is the soil permeability; and γ_w is the unit weight of water.

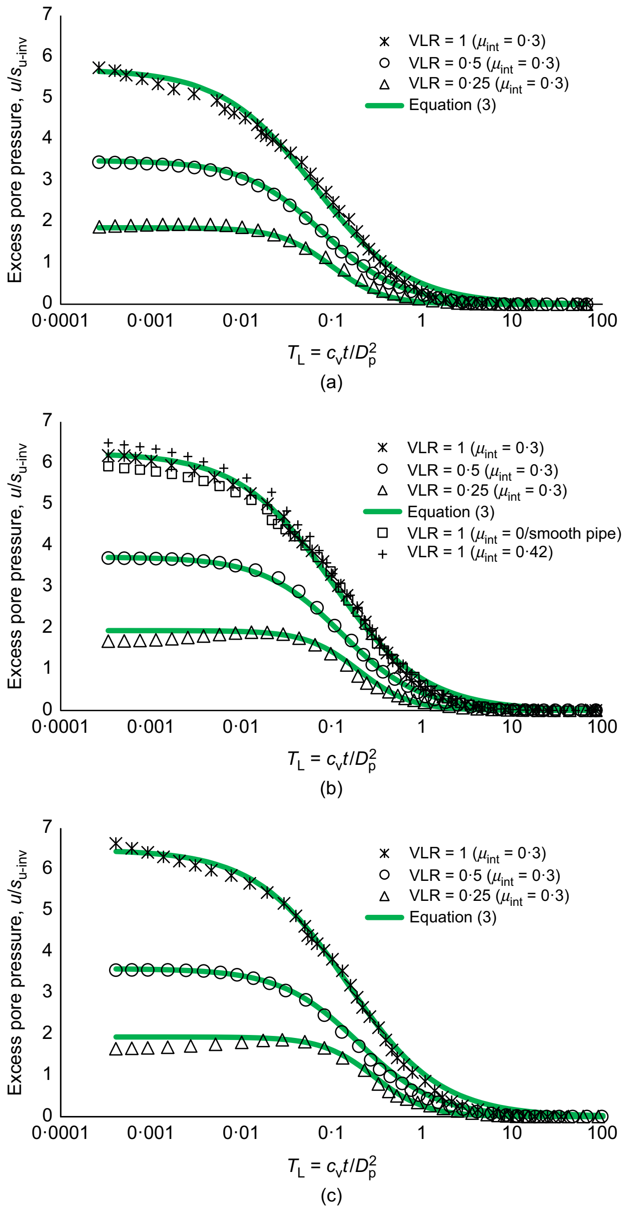

Fig. 7. Laying-induced excess pore pressure dissipation at the pipe invert for different embedment depths and VLRs. Solid lines represent fitted curves: (a) $z/D_p = 0{\cdot}3$; (b) $z/D_p = 0{\cdot}5$; (c) $z/D_p = 0{\cdot}7$

COMPARISON WITH CENTRIFUGE MODEL DATA AND RESULTS OF PREVIOUS STUDIES

Penetration and consolidation response

Figure 6 shows the computed and measured penetration resistance V normalised by the undrained soil strength at the pipe invert and pipe diameter, hereafter termed the normalised penetration resistance, plotted against the diameter-normalised depth, from the current study and some previous studies. The study by Ullah *et al.* (2018) was conducted using a coupled-consolidation 3D RITSS analysis with an effective stress Mohr–Coulomb model. The studies by Tian *et al.* (2014) and Wang *et al.* (2010) were conducted using total stress plane strain RITSS analysis, while the studies by Dutta *et al.* (2015) were conducted using total stress coupled Eulerian–Lagrangian analysis. The load–penetration curves are narrowly banded up to an embedment depth of $0{\cdot}1D_p$. At larger depths, the results of Wang *et al.* (2010), Tian *et al.* (2014) and Dutta *et al.* (2015) showed slightly lower normalised penetration resistances compared to the current RITSS analysis. This can be attributed to the differences in the constitutive models and interface friction coefficients (μ_{int}) used. In particular, the Mohr–Coulomb and Tresca models in the previous computational studies assumed a hexagonal 3D generalisation, whereas the Cam Clay model used herein assumes a circular generalisation. Notwithstanding this, the discrepancy between the different analyses did not exceed ~5%. The results from the 3D RITSS analyses conducted herein show that increasing the interface friction coefficient has a significant effect on the results. The centrifuge model data fall between the curves for interface friction coefficients of 0·3 and 0·42. The case of a fully rough pipe was modelled using an interface friction coefficient of 0·532, which corresponds to a friction angle of 28°. The latter value corresponds to the plane-strain friction angle for M of

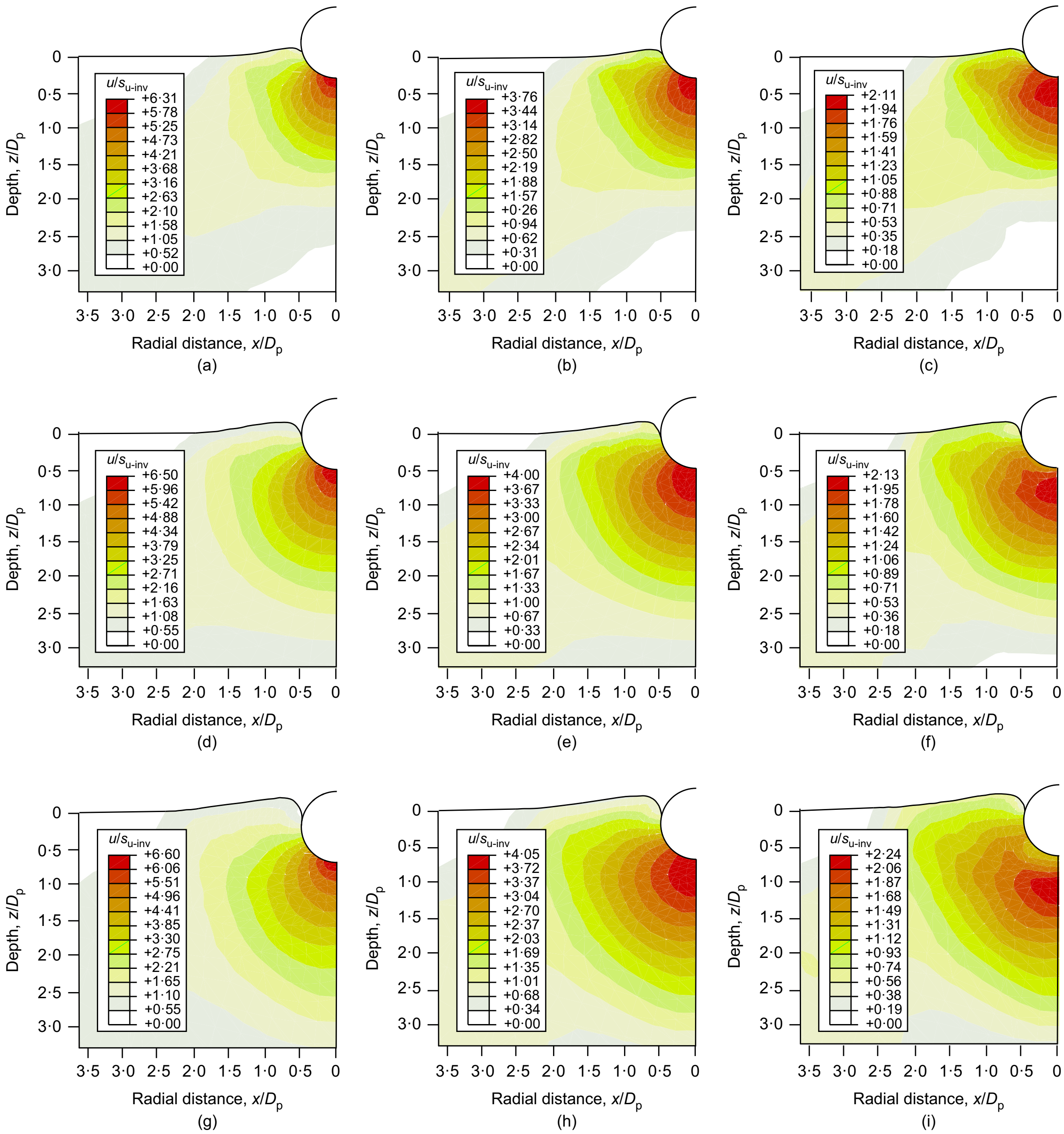

Fig. 8. The excess pore pressure (normalised by undrained strength at the invert, $s_{u\text{-}inv}$) beneath the pipe immediately after penetration for $\mu_{int} = 0{\cdot}3$: (a) $z/D_p = 0{\cdot}3$, VLR = 1; (b) $z/D_p = 0{\cdot}3$, VLR = 0·5; (c) $z/D_p = 0{\cdot}3$, VLR = 0·25; (d) $z/D_p = 0{\cdot}5$, VLR = 1; (e) $z/D_p = 0{\cdot}5$, VLR = 0·5; (f) $z/D_p = 0{\cdot}7$, VLR = 0·25; (g) $z/D_p = 0{\cdot}7$, VLR = 1; (h) $z/D_p = 0{\cdot}7$, VLR = 0·5; (i) $z/D_p = 0{\cdot}7$, VLR = 0·25

Table 3. ξ_0, A and m of laying-induced excess pore pressure dissipation curves for $\mu_{int} = 0{\cdot}3$

	$z/D_p = 0{\cdot}3$			$z/D_p = 0{\cdot}5$			$z/D_p = 0{\cdot}7$		
	ξ_0	A	m	ξ_0	A	m	ξ_0	A	m
VLR = 1	5·7	0·065	0·85	6·2	0·1	0·85	6·5	0·15	0·85
VLR = 0·5	3·5	0·08	1	3·7	0·13	1	3·6	0·2	1
VLR = 0·25	1·8	0·1	1·5	1·9	0·2	1·5	1·9	0·3	1·5

0·9 (Chang *et al.*, 1999). On the other hand, the influence of the compression and swelling indices, λ and κ, on the normalised penetration resistance is relatively minimal.

Figure 7 shows the excess pore pressure at the pipe invert at different dimensionless times after the desired pipe embedment depth is reached. The dimensionless time T_L is defined by

$$T_L = \frac{c_v t}{D_p^2} \tag{2}$$

where t is the time lapse after completion of the pipe embedment. The excess pore pressure u is normalised by the initial undrained shear strength of the soil at the pipe invert. As Fig. 7 shows, for VLR of 1 and 0·5, the excess pore pressure dissipates monotonically after pipe penetration. However, for VLR of 0·25, there is an initial transient

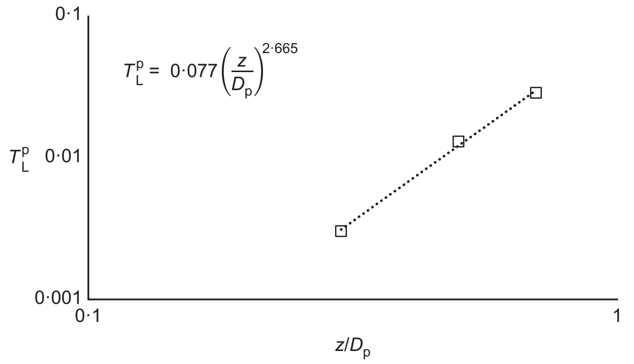

Fig. 9. Dimensionless time to peak excess pore pressure at the invert for VLR of 0·25 and $\mu_{int} = 0{\cdot}3$

increase in excess pore pressure. This can be explained by the location of the maximum excess pore pressure. As Fig. 8 shows, for VLR of 1 and 0·5, the zone of highest excess pore pressure lies just beneath the pipe invert. This generates an outward and downward flow of pore water. For VLR of 0·25, the zone of highest excess pore pressure lies deeper in the soil. This causes pore water to equilibrate towards the pipe invert, resulting in a transient pore pressure increase. Krost *et al.* (2011) reported a similar trend at the centre-line of a strip footing due to the high concentration of excess pore pressures close to the edges. Yan *et al.* (2017) also reported similar behaviour of excess pore pressure beneath toroid and ball penetrometers. As Fig. 7(b) shows, a rough pipe–soil interface generates slightly higher laying-induced excess pore pressure at the invert compared to a smooth pipe. However, this slight difference is only apparent shortly after pipe penetration, and the subsequent consolidation curves remain tightly banded.

The laying-induced excess pore pressure dissipation at the invert can be fitted approximately by a relationship of the form

$$\xi = \frac{\xi_0}{1 + (T^*/A)^m} \tag{3}$$

where ξ_0 is the normalised excess pore pressure ($u/s_{u\text{-inv}}$) at the invert immediately after penetration and application of the pipe weight. The parameter A is the dimensionless time at which the invert pore pressure ξ has decreased to half of its initial value, ξ_0, and m is a fitted index. Equation (3) does not capture the initial rise in excess pore pressure at the invert for VLR of 0·25. Instead, the value of ξ_0 is taken to be the peak pore pressure. The fitted parameters are summarised in Table 3. For VLR of 0·25, the dimensionless time to peak T_L^p

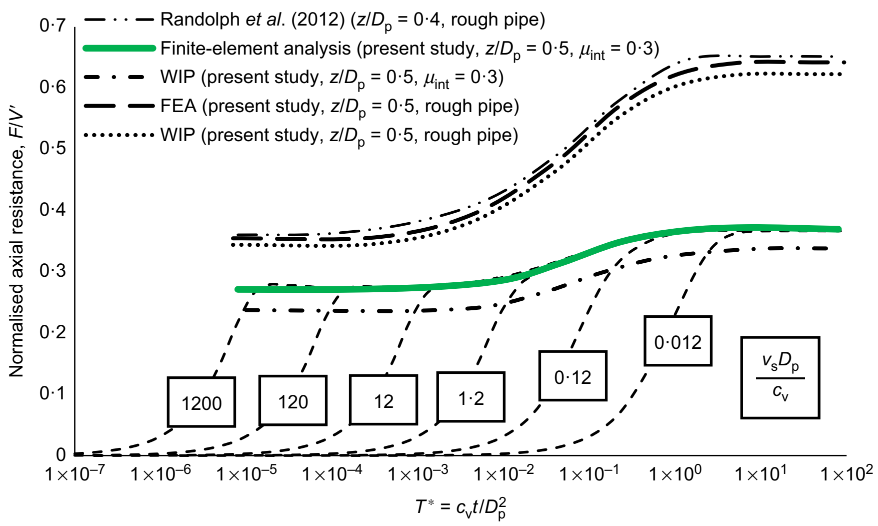

Fig. 10. Axial pipe–soil resistance of the Randolph *et al.* (2012) WIP analysis, finite-element analysis (present study) and WIP (present study) for VLR = 1

of the initial rise in excess pore pressure at the invert can be fitted by (Fig. 9)

$$T_L^p = 0.077\left(\frac{z}{D_p}\right)^{2.665} \tag{4}$$

Axial sliding

Figure 10 shows the computed results of the axial pipe resistance F normalised by the pipe weight V', plotted against the dimensionless time T^* for various dimensionless velocities V_s. Following Randolph *et al.* (2012), the

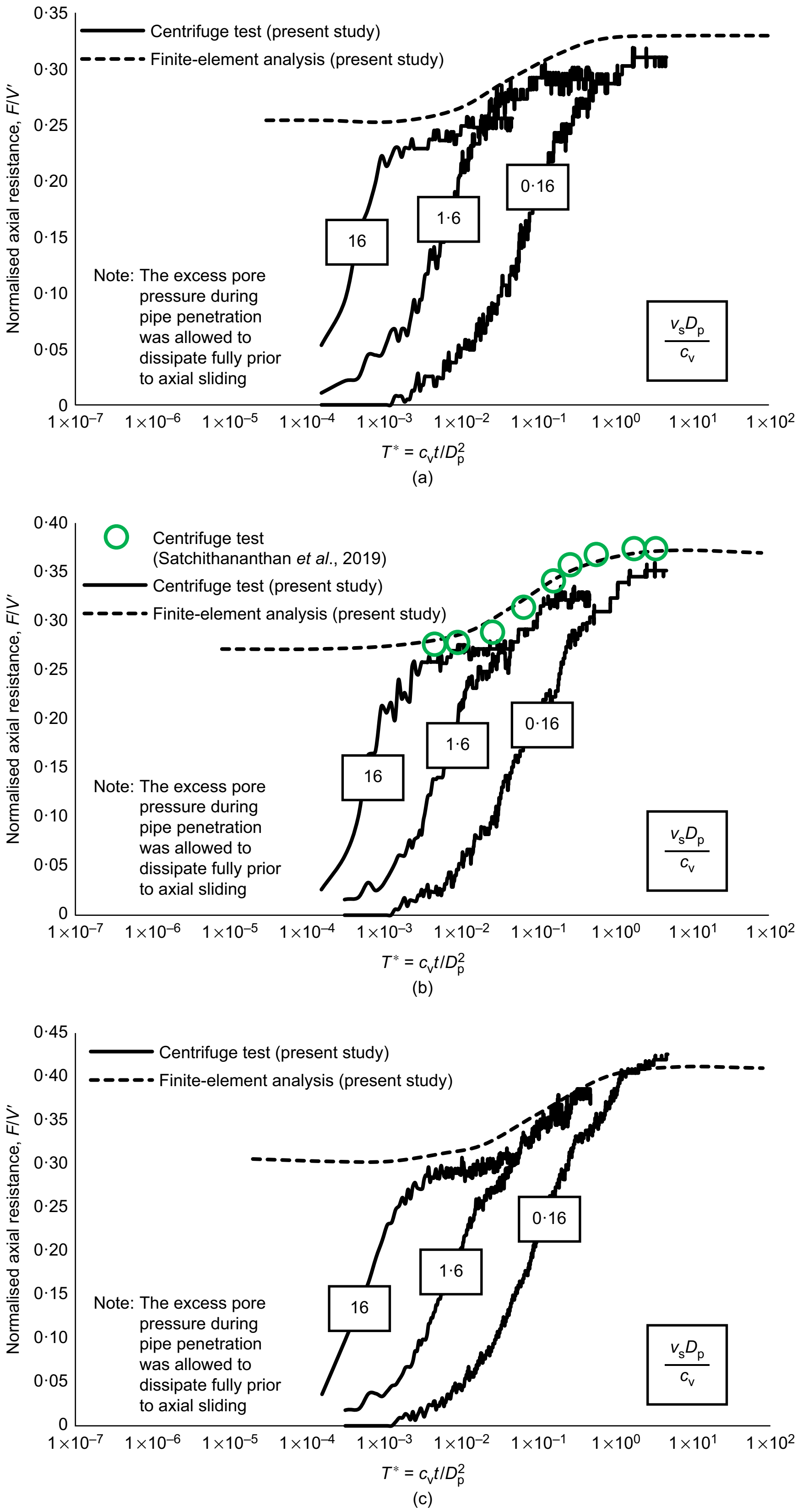

Fig. 11. Normalised axial resistance of the current finite-element analysis with centrifuge tests at different embedment depths for VLR = 1 and $\mu_{int} = 0.3$

dimensionless time T^* and velocity V_s are defined by

$$T^* = \frac{c_v t^*}{D_p^2}, \; V_s = \frac{v_s D_p}{c_v} \tag{5}$$

where t^* is the elapsed time from the start of the axial sliding and v_s is the sliding velocity. As Fig. 10 shows, the backbone curves for terminal shearing resistance are similar in shape to that reported by Randolph *et al*. (2012). In all cases, the ratio of sliding resistance to pipe weight drops below the pipe–soil coefficient of friction for very fast sliding corresponding to the undrained situation, owing to the sliding-induced excess pore pressure. The main difference is the lower normalised axial resistance F/V' in the current analysis. Using an interface friction coefficient of 0·532, corresponding to a fully rough pipe, produces much better agreement with the analysis by Randolph *et al*. (2012). In addition, as Fig. 11 shows, the RITSS results agree well with the centrifuge model results of Satchithananthan *et al*. (2019), as well as those obtained herein.

Figure 10 also shows the results from a WIP analysis using the same soil properties and boundary conditions as those for the RITSS analysis (Table 2). Following Randolph *et al*. (2012), after the initial geostatic step, the WIP pipe was further penetrated vertically by a depth increment of $0{\cdot}1D_p$ so as to mobilise the ultimate penetration resistance at the pre-embedded depth. The excess pore pressure generated was allowed to fully dissipate under a constant pipe weight equivalent to the mobilised penetration resistance. The pipe was then displaced axially in the same way as in the RITSS analyses. As Fig. 6 shows, for the same interface friction coefficient, the mobilised penetration resistance at the pre-embedded depth is approximately 14% less than that obtained from the RITSS analysis. The sliding resistance of the WIP pipe is also consistently lower than that of the RITSS installed pipe, with the difference being approximately constant (see Fig. 10). This is because the WIP model computes lower normalised mean effective stress beneath the pipe prior to axial sliding (see Fig. 12). The zone of excess pore pressure for the WIP pipe immediately after penetration is also smaller in extent compared to the RITSS installed pipe (see Fig. 13). This indicates that the higher penetration resistance from the RITSS analysis can be attributed to the additional soil weight arising from soil heave on both sides of the pipe and the flow of stronger soil from larger depth upwards around the pipe circumference. The soil flow in the RITSS analysis displaces the soil with pre-accumulated excess pore pressures further outwards and away from the pipe, resulting in a larger excess pore pressure zone compared to the WIP analysis. During undrained axial sliding, both

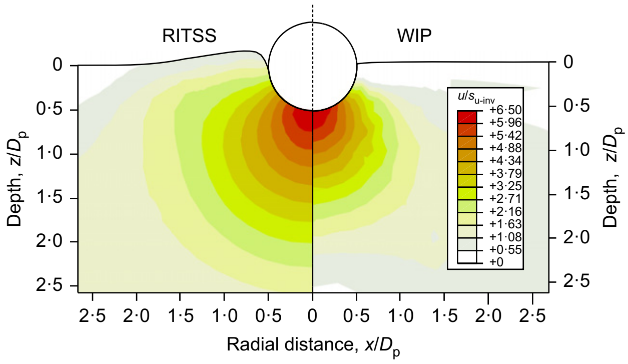

Fig. 13. Excess pore pressure (normalised by undrained strength at the invert, $s_{u\text{-inv}}$) beneath the pipe immediately after penetration at $0{\cdot}5D_p$ for VLR = 1 and $\mu_{int} = 0{\cdot}3$

WIP and RITSS models give similar excess pore pressure distributions around the pipe (see Fig. 14). However, owing to the lower mean effective stress around the pipe circumference prior to axial sliding, the normalised axial resistance is lower in the WIP analysis than in the RITSS analysis (see Fig. 10).

Figure 15 shows the normalised excess pore pressure changes in the zone of highest sliding-induced excess pore pressure during axial sliding. For all dimensionless velocities, the excess pore pressure increased from the beginning of axial sliding to a peak value, followed by dissipation. This is similar to the pore pressure response reported by Satchithananthan *et al*. (2019) based on centrifuge tests, and indicates that towards the later stage of sliding, pore pressure dissipation outpaces generation. The peak pore pressure decreases significantly as sliding velocity decreases. The post-peak segments of the excess pore pressure curves collapse into a narrow backbone curve. The left-hand end of this backbone curve represents the excess pore pressure generated under near-undrained conditions at very high sliding velocity, while the falling segment corresponds to pore pressure dissipation. Hence, this backbone curve represents the dissipation characteristics of the excess pore pressure beneath the pipe. Excess pore pressure will rise to some point on this curve before dissipating. Higher sliding velocity will cause a more rapid rise in excess pore pressure, thus allowing a higher point on the backbone curve to be reached.

Figure 16 shows the excess pore pressure contours at the instant of peak sliding-induced excess pore pressure during fast axial sliding for different embedment depth ratios and

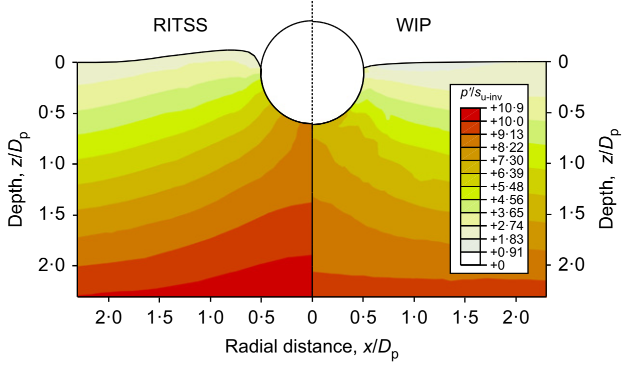

Fig. 12. Mean effective stress (normalised by undrained strength at the invert, $s_{u\text{-inv}}$) beneath the pipe after penetration and consolidation at $0{\cdot}5D_p$ for VLR = 1 and $\mu_{int} = 0{\cdot}3$

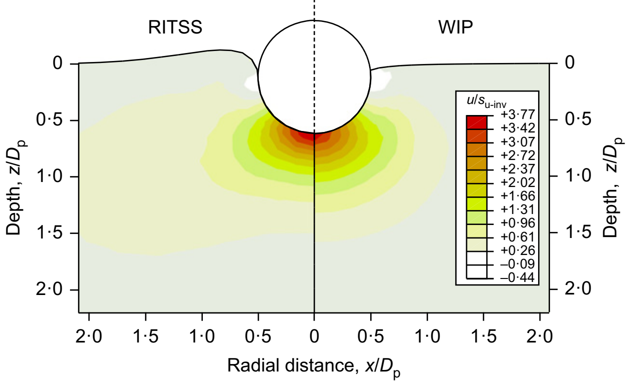

Fig. 14. Excess pore pressure (normalised by undrained strength at the invert, $s_{u\text{-inv}}$) during undrained axial sliding at $T^* = 5{\cdot}2 \times 10^{-5}$ for $v_s D_p/c_v = 11\ 900$, VLR = 1 and $\mu_{int} = 0{\cdot}3$

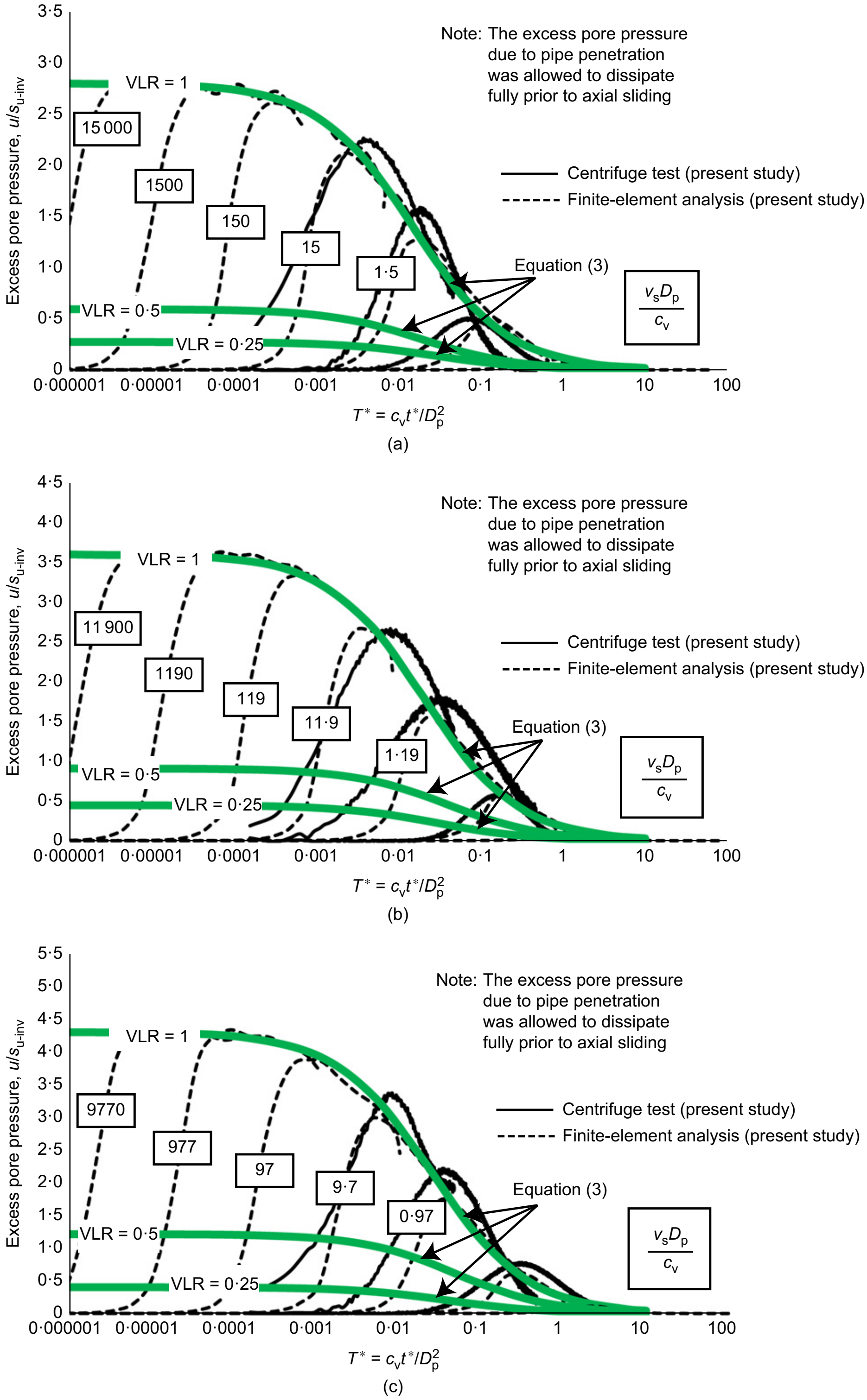

Fig. 15. Excess pore pressure (at the zone of highest sliding-induced excess pore pressure) during axial sliding for $\mu_{int} = 0{\cdot}3$: (a) $z/D_p = 0{\cdot}3$; (b) $z/D_p = 0{\cdot}5$; (c) $z/D_p = 0{\cdot}7$

VLRs. For VLRs of 1·0 and 0·5, the zone of highest sliding-induced excess pore pressure lies just beneath the pipe. However, for VLR of 0·25, the zone of highest sliding-induced excess pore pressure lies above the pipe invert (Fig. 16). The peak excess pore pressure during axial sliding also coincides approximately with the point of intersection of the rising segment and a narrowly banded backbone curve. The backbone curves for the variation of excess pore pressure shown in Fig. 15 (corresponding to the zone of highest sliding-induced excess pore pressure) can be modelled by equation (3), but with the values of the parameters ξ_0, A and m as shown in Table 4. Finally, as Fig. 17 shows, the dimensionless time to peak sliding-induced excess pore pressure T_p^* can be related to the dimensionless sliding velocity V_s by an equation of the form

$$T_p^* = \mathrm{X}\, V_s^{-0{\cdot}9} \tag{6}$$

where X values for different embedment depths and VLRs are summarised in Table 5. Overall, the dissipation trends of

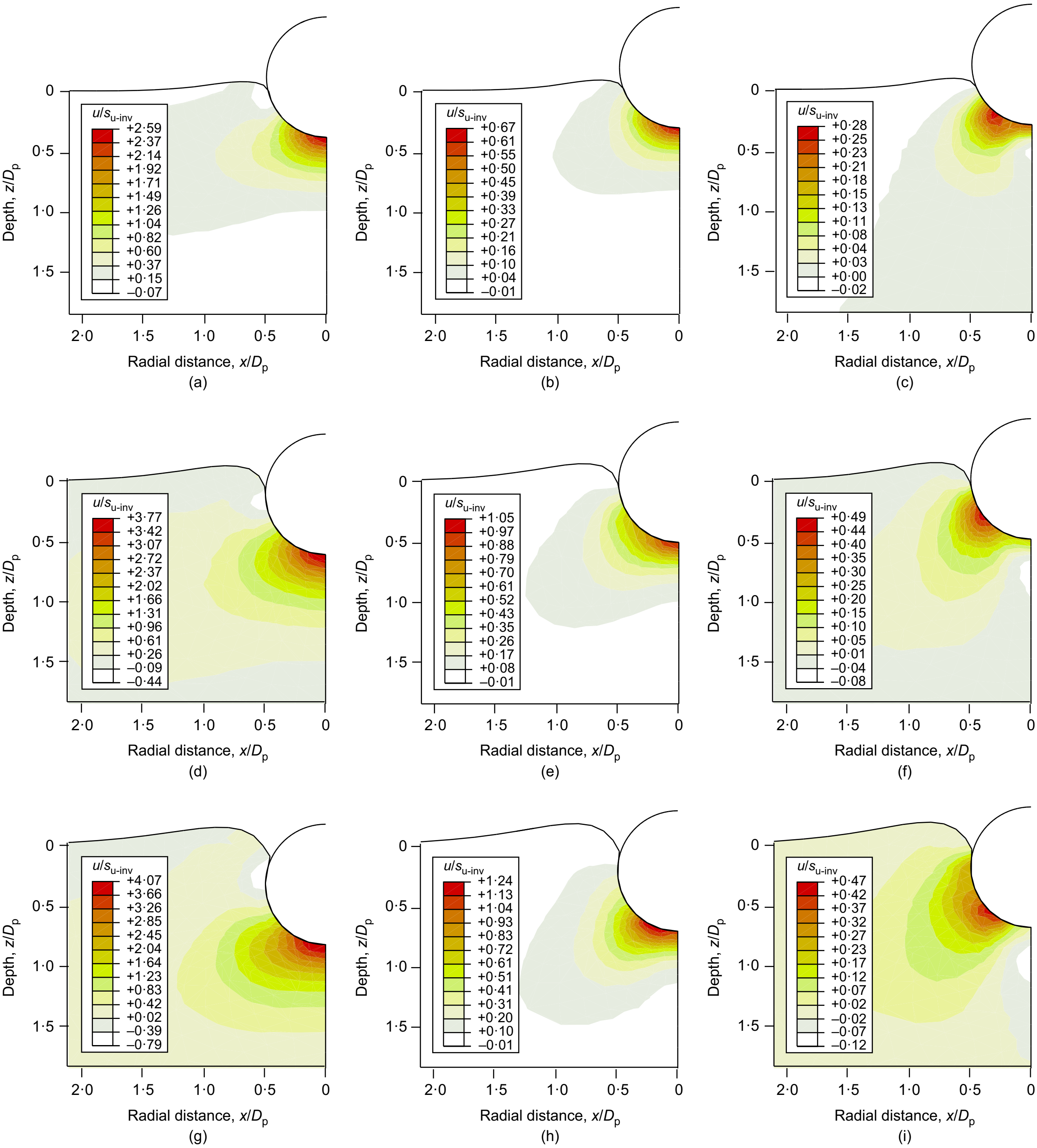

Fig. 16. Excess pore pressure contours at T_p^* (i.e. the instant of peak excess pore pressure at the zone of highest shear-induced excess pore pressure), under very high sliding velocity (i.e. undrained conditions) for $\mu_{int} = 0{\cdot}3$: (a) $z/D_p = 0{\cdot}3$, VLR = 1 at $T_p^* = 3{\cdot}42 \times 10^{-6}$ and $V_s = 15\,000$; (b) $z/D_p = 0{\cdot}3$, VLR = 0·5 at $T_p^* = 2{\cdot}31 \times 10^{-6}$ and $V_s = 15\,000$; (c) $z/D_p = 0{\cdot}3$, VLR = 0·25 at $T_p^* = 1{\cdot}63 \times 10^{-6}$ and $V_s = 15\,000$; (d) $z/D_p = 0{\cdot}5$, VLR = 1 at $T_p^* = 5{\cdot}22 \times 10^{-6}$ and $V_s = 11\,900$; (e) $z/D_p = 0{\cdot}5$, VLR = 0·5 at $T_p^* = 3{\cdot}07 \times 10^{-6}$ and $V_s = 11\,900$; (f) $z/D_p = 0{\cdot}7$, VLR = 0·25 at $T_p^* = 2{\cdot}25 \times 10^{-6}$ and $V_s = 11\,900$; (g) $z/D_p = 0{\cdot}7$, VLR = 1 at $T_p^* = 1{\cdot}53 \times 10^{-5}$ and $V_s = 9770$; (h) $z/D_p = 0{\cdot}7$, VLR = 0·5 at $T_p^* = 3{\cdot}33 \times 10^{-5}$ and $V_s = 9770$; (i) $z/D_p = 0{\cdot}7$, VLR = 0·25 at $T_p^* = 2{\cdot}40 \times 10^{-5}$ and $V_s = 9770$

Table 4. ξ_0, A and m of sliding-induced excess pore pressure curves for $\mu_{int} = 0{\cdot}3$

	$z/D_p = 0{\cdot}3$			$z/D_p = 0{\cdot}5$			$z/D_p = 0{\cdot}7$		
	ξ_0	A	m	ξ_0	A	m	ξ_0	A	m
VLR = 1	2·8	0·015	0·75	3·6	0·02	0·75	4·3	0·025	0·75
VLR = 0·5	0·59	0·03	0·75	0·91	0·04	0·75	1·22	0·05	0·75
VLR = 0·25	0·27	0·02	0·75	0·45	0·03	0·75	0·41	0·04	0·75

the laying- and sliding-induced excess pore pressure are similar; the main difference is that the latter is much lower and dissipates much faster, Tables 3 and 4.

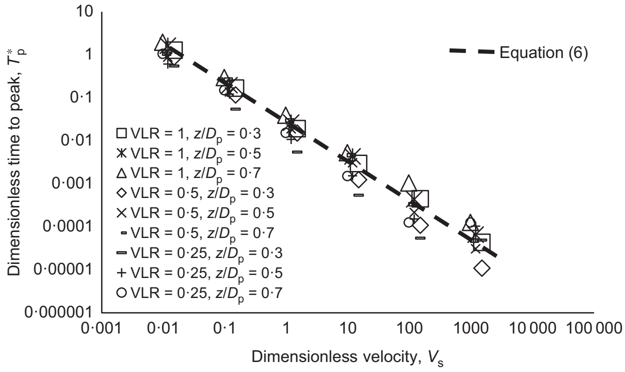

Fig. 17. Time to peak T_p^* plotted against dimensionless velocity V_s for μ_{int} = 0·3

Table 5. The X parameter for different embedment depths and VLRs, for μ_{int} = 0·3

	$z/D_p = 0{\cdot}3$	$z/D_p = 0{\cdot}5$	$z/D_p = 0{\cdot}7$
VLR = 1	0·03	0·038	0·043
VLR = 0·5	0·015	0·019	0·022
VLR = 0·25	0·007	0·01	0·012

PROPOSED METHOD FOR ESTIMATING AXIAL PIPE–SOIL FRICTION

As Fig. 18 shows, the effective normal contact stresses around the pipe circumference after penetration and consolidation are significantly affected by the embedment depth and VLR. The maximum normal contact stress occurs at the invert and decreases towards the soil surface. In drained shearing, the axial resistance F_d can be expressed in terms of the normal contact stresses around the pipe circumference as

$$F_d = 2\int_0^{\theta_{ce}} \mu_{int}\sigma_n' r \, d\theta = \mu_{int} s_{u\text{-}inv} D_p S \tag{7a}$$

in which

$$S = \int_0^{\theta_{ce}} \frac{\sigma_n'}{s_{u\text{-}inv}} \, d\theta \tag{7b}$$

where σ_n' is the effective normal contact stress around the pipe circumference after penetration and consolidation; μ_{int} is the pipe–soil interface friction coefficient; and θ_{ce} is the maximum circumferential pipe–soil contact angle measured in radians. For a given depth of embedment and vertical load ratio, the profiles of effective contact stress at the pipe circumference normalised by the undrained shear strength of the soil are tightly banded for different values of the internal coefficient of friction, M, compression index, λ, and swelling index, κ, of the soil (see Fig. 18). This indicates that normalising the effective contact stress by the undrained shear strength of the soil at the invert removes much of the variation arising from variations in M, λ and κ, and allows the effective contact stress corresponding to each depth of

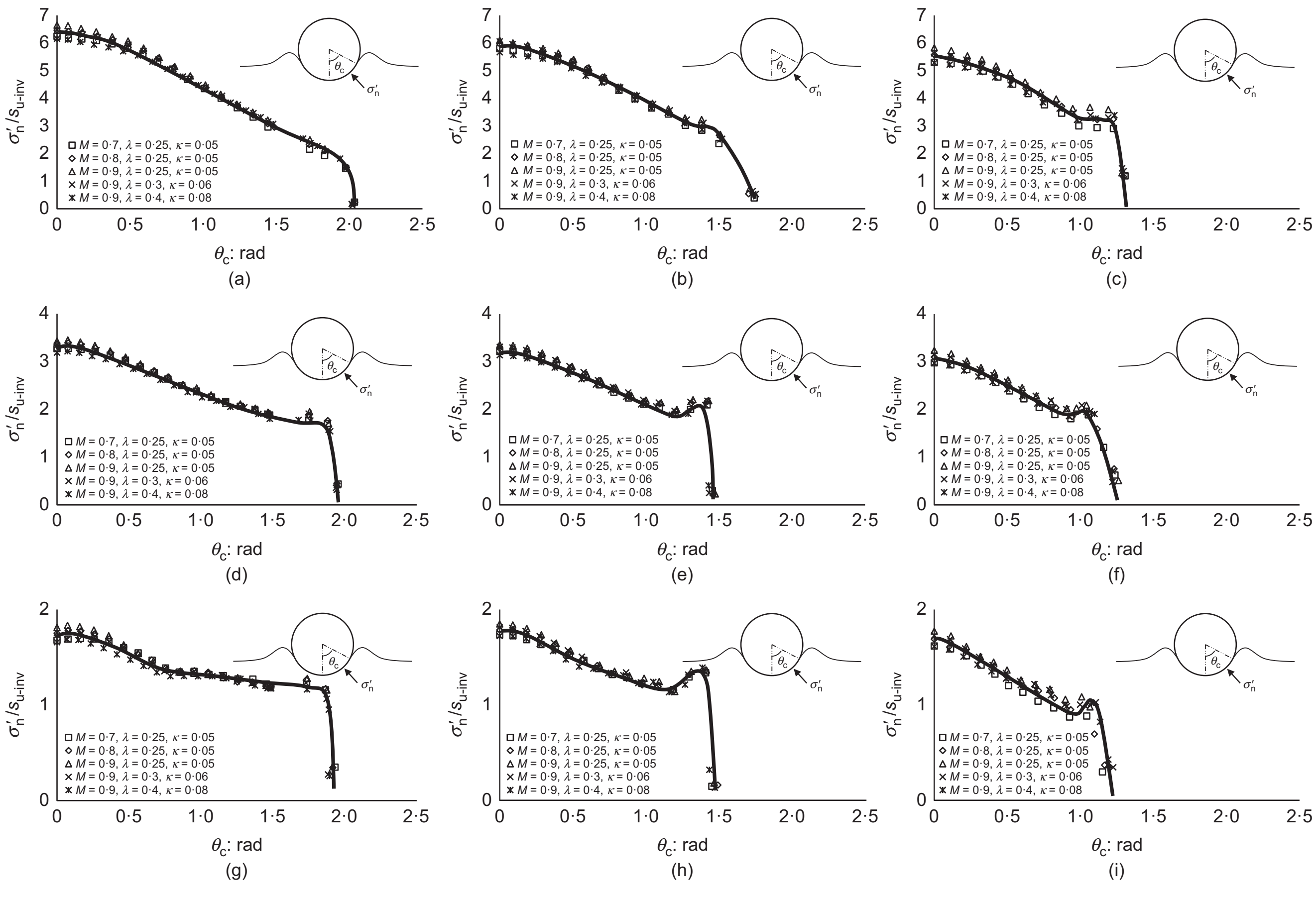

Fig. 18. Effective normal contact stresses around the pipe circumference for μ_{int} = 0·3 (normalised by undrained strength at the invert, $s_{u\text{-}inv}$) after penetration and consolidation (i.e. at T^* = 0): (a) z/D_p = 0·7, VLR = 1; (b) z/D_p = 0·5, VLR = 1; (c) z/D_p = 0·3, VLR = 1; (d) z/D_p = 0·7, VLR = 0·5; (e) z/D_p = 0·5, VLR = 0·5; (f) z/D_p = 0·3, VLR = 0·5; (g) z/D_p = 0·7, VLR = 0·25; (h) z/D_p = 0·5, VLR = 0·25; (i) z/D_p = 0·3, VLR = 0·25

penetration and vertical load ratio to be approximated by a single curve (see Fig. 18).

For undrained conditions, the axial resistance F_u can be expressed as

$$F_u = 2\int_0^{\theta_{ce}} \mu_{int}(\sigma_n' - u) r \, d\theta = F_d - \mu_{int} s_{u\text{-}inv} D_p U \tag{8a}$$

in which

$$U = \int_0^{\theta_{ce}} \frac{u}{s_{u\text{-}inv}} \, d\theta \tag{8b}$$

where u is the excess pore pressure around the pipe circumference. Fig. 19 shows the sliding-induced excess pore pressure around the pipe circumference, normalised by the invert undrained shear strength, for fast axial sliding (i.e. undrained condition) at time T_p^*. The normalised excess pore pressure shows slightly larger scatter than the effective contact stresses, especially for a depth of embedment $z/D_p \geq 0{\cdot}5$ and vertical load ratio $\leq 0{\cdot}5$. Nonetheless, the profiles are still sufficiently narrowly banded to be approximated by a single curve, as shown in Fig. 19. Hence, if the undrained strength at the invert is known, the integral terms corresponding to the effective normal contact stress (equation (7b)) and sliding-induced excess pore pressure (equation (8b)) can be estimated based on the area under the curves shown in Figs 18 and 19, respectively. The values of S and U for the representative curves are summarised in Table 6.

Figure 20(a) shows the values of S and U when normalised by the respective values of the same variable for VLR of 1·0, termed herein as S_0 and U_0. The curves of S/S_0 are tightly banded and can be fitted by an equation of the form

$$\frac{S}{S_0} = R^{0{\cdot}9} \tag{9}$$

where R is the vertical load ratio. The curves of U/U_0 are slightly more scattered, but can still be approximated by an equation of the form

$$\frac{U}{U_0} = R^{1{\cdot}15} \tag{10}$$

Furthermore, as Fig. 20(b) shows, S_0 and U_0 can be correlated to the normalised depth of embedment by the relations

$$S_0 = 10{\cdot}5\left(\frac{z}{D_p}\right)^{0{\cdot}5} \tag{11a}$$

$$U_0 = 3{\cdot}1\left(\frac{z}{D_p}\right)^{0{\cdot}7} \tag{11b}$$

Combining equations (9)–(11) leads to

$$S = 10{\cdot}5\left(\frac{z}{D_p}\right)^{0{\cdot}5} R^{0{\cdot}9} \tag{12a}$$

$$U = 3{\cdot}1\left(\frac{z}{D_p}\right)^{0{\cdot}7} R^{1{\cdot}15} \tag{12b}$$

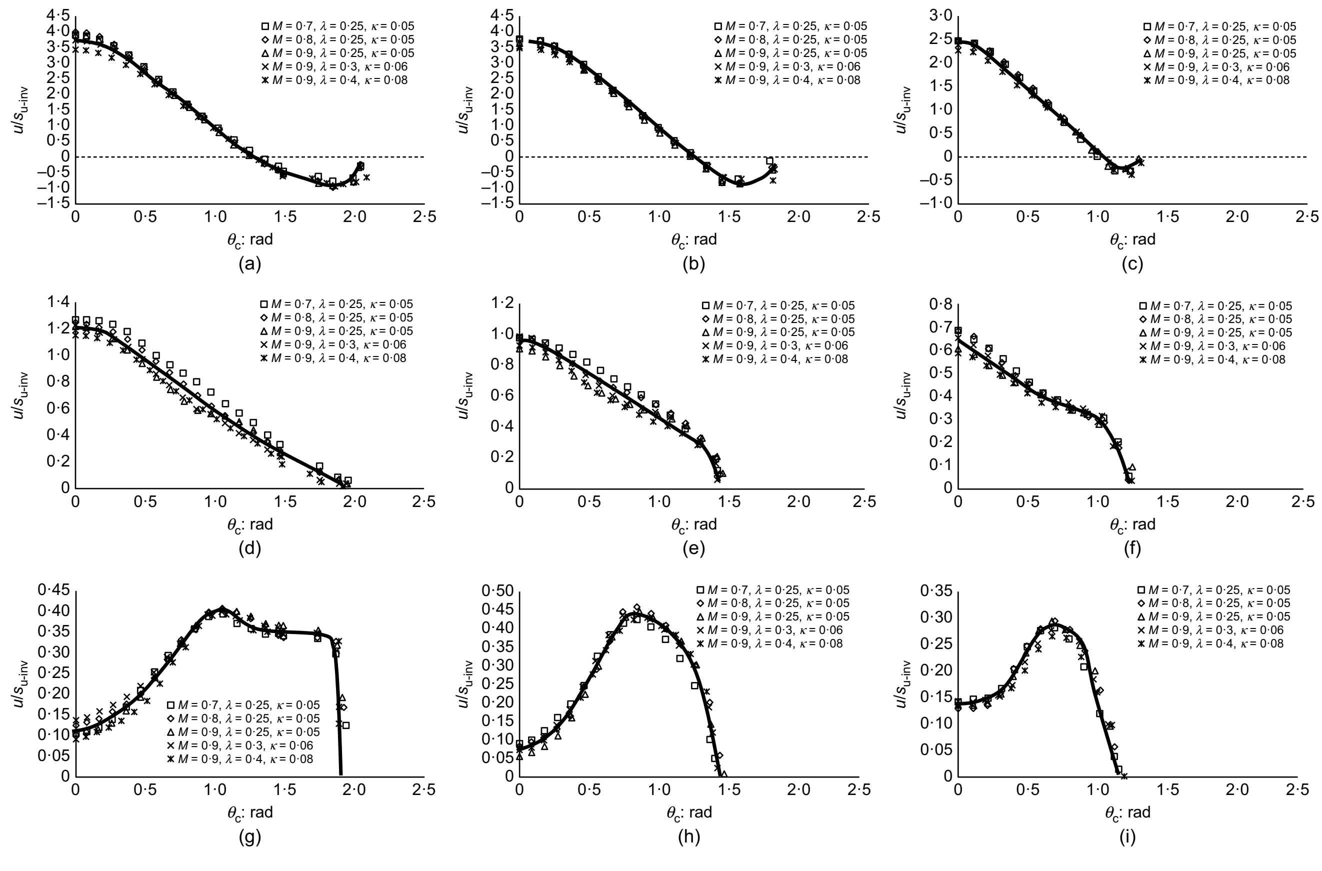

Fig. 19. Shear-induced excess pore pressure around the pipe circumference for $\mu_{int} = 0{\cdot}3$ (normalised by undrained strength at the invert, $s_{u\text{-}inv}$) for very fast axial sliding (i.e. undrained condition) at time T_p^*: (a) $z/D_p = 0{\cdot}7$, VLR = 1 at $T_p^* = 1{\cdot}53 \times 10^{-5}$ and $V_s = 9770$; (b) $z/D_p = 0{\cdot}5$, VLR = 1 at $T_p^* = 5{\cdot}22 \times 10^{-6}$ and $V_s = 11\,900$; (c) $z/D_p = 0{\cdot}3$, VLR = 1 at $T_p^* = 3{\cdot}42 \times 10^{-6}$ and $V_s = 15\,000$; (d) $z/D_p = 0{\cdot}7$, VLR = 0·5 at $T_p^* = 3{\cdot}33 \times 10^{-5}$ and $V_s = 9770$; (e) $z/D_p = 0{\cdot}5$, VLR = 0·5 at $T_p^* = 3{\cdot}07 \times 10^{-6}$ and $V_s = 11\,900$; (f) $z/D_p = 0{\cdot}3$, VLR = 0·5 at $T_p^* = 2{\cdot}31 \times 10^{-6}$ and $V_s = 15\,000$; (g) $z/D_p = 0{\cdot}7$, VLR = 0·25 at $T_p^* = 2{\cdot}40 \times 10^{-5}$ and $V_s = 9770$; (h) $z/D_p = 0{\cdot}5$, VLR = 0·25 at $T_p^* = 2{\cdot}25 \times 10^{-6}$ and $V_s = 11\,900$; (i) $z/D_p = 0{\cdot}3$, VLR = 0·25 at $T_p^* = 1{\cdot}63 \times 10^{-6}$ and $V_s = 15\,000$

Table 6. Integral values corresponding to the normalised effective normal contact stress and sliding-induced excess pore pressure around the pipe circumference for $\mu_{\text{int}} = 0{\cdot}3$

z/D_p	VLR	$S = \int_0^{\theta_{ce}} \sigma'_n / s_{u\text{-inv}}\, d\theta$	$U = \int_0^{\theta_{ce}} u / s_{u\text{-inv}}\, d\theta$
0·7	1	8·918	2·335
	0·5	4·879	1·146
	0·25	2·709	0·564
0·5	1	7·313	2·060
	0·5	3·829	0·860
	0·25	2·115	0·386
0·3	1	5·769	1·291
	0·5	2·988	0·496
	0·25	1·535	0·235

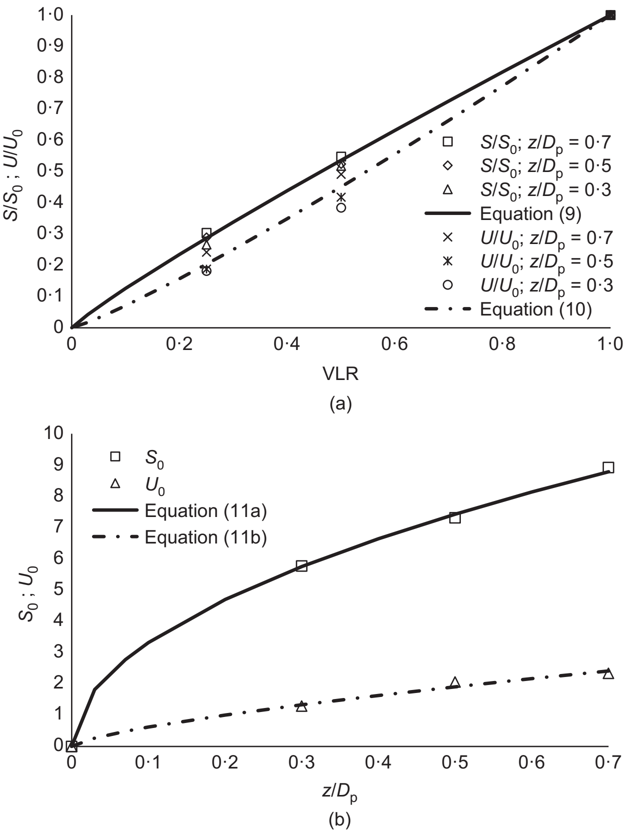

Fig. 20. (a) Normalised integral values of contact stresses and shear-induced excess pore pressures – that is, S/S_0; U/U_0 – plotted against VLR; (b) Integral values of contact stresses and shear-induced excess pore pressures for VLR = 1 – that is, S_0; U_0 – plotted against z/D_p

EMBEDMENT ENHANCEMENT FACTOR

White & Randolph (2007) and Ansari *et al.* (2014) proposed an enhancement factor to account for the higher sliding resistance under drained conditions, wherein the pipe velocity is sufficiently slow that excess pore pressures do not accumulate. This is defined as the integral of the post-laying effective contact stress over the embedded circumference of the pipe, normalised by the pipe weight. The embedment enhancement factor ζ_d can be expressed as

$$\zeta_d = \frac{2\int_0^{\theta_{ce}} \sigma'_n r\, d\theta}{V'} = \frac{F_d}{\mu_{\text{int}} V'} \tag{13}$$

As Fig. 21 shows, for the same normalised embedment depth, White & Randolph's (2007) enhancement factors are

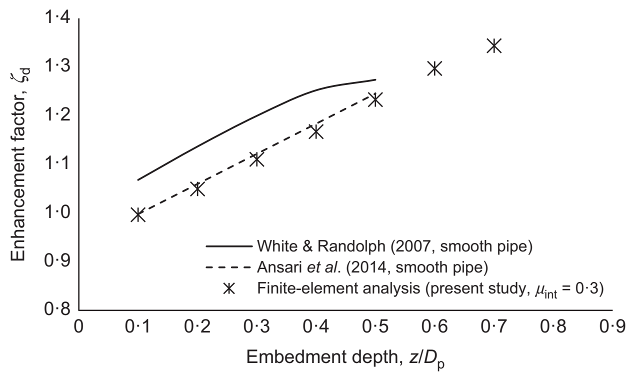

Fig. 21. The enhancement factors at different embedment depths for VLR = 1

higher than those of Ansari *et al.* (2014) and the present study. This can be attributed to the fact that White & Randolph (2007) assumed a uniform stress distribution around the pipe circumference. As Fig. 12 shows, the maximum effective stress is observed at the invert and decreases significantly towards the soil surface. Hence, assuming a uniform stress distribution around the pipe circumference overestimates the enhancement factor, and thus the axial sliding resistance.

Combining equations (7a), (12a) and (13) leads to

$$\zeta_d = \frac{10{\cdot}5 s_{u\text{-inv}} (zD_p)^{0{\cdot}5} R^{0{\cdot}9}}{V'} \tag{14}$$

An 'undrained' enhancement factor ζ_u can also be defined for very fast sliding by

$$\zeta_u = \frac{F_u}{\mu_{\text{int}} V'} \tag{15}$$

Combining equations (8a), (12b) and (14) leads to

$$\zeta_u = \zeta_d - \frac{3{\cdot}1 s_{u\text{-inv}} z^{0{\cdot}7} D_p^{0{\cdot}3} R^{1{\cdot}15}}{V'} \tag{16}$$

The undrained enhancement factor is often less than 1·0 owing to the effect of the sliding-induced excess pore pressure. This is consistent with Fig. 10 in which the undrained sliding resistance often falls below $\mu_{\text{int}} V'$.

Equations (14) and (16) are fitted using results for a pipe with an interface friction coefficient of 0·3. Nonetheless, as Fig. 22 shows, the normalised effective contact stress profiles around the pipe circumference are not significantly affected by the interface friction coefficient. This mirrors the laying-induced excess pore pressure (Fig. 7), which is also not strongly affected by the interface friction coefficient. It is also akin to the observation by Hossain *et al.* (2006) that, in spudcan penetration, spudcan–soil friction does not appear to significantly affect the cavity depth and bearing capacity factor. This suggests that, for some problems involving penetration of bluff bodies into soft soil, interface friction may not have a significant effect on the post-penetration behaviour. Thus, the integral values predicted by equations (11a) and (12a), and the corresponding equation for drained enhancement factor ζ_d (equation (14)) remain valid for the different friction coefficients that may be encountered in practice.

On the other hand, the sliding-induced excess pore pressure during fast axial sliding is significantly affected by the interface friction coefficient, with a higher interface friction coefficient generating higher excess pore pressure

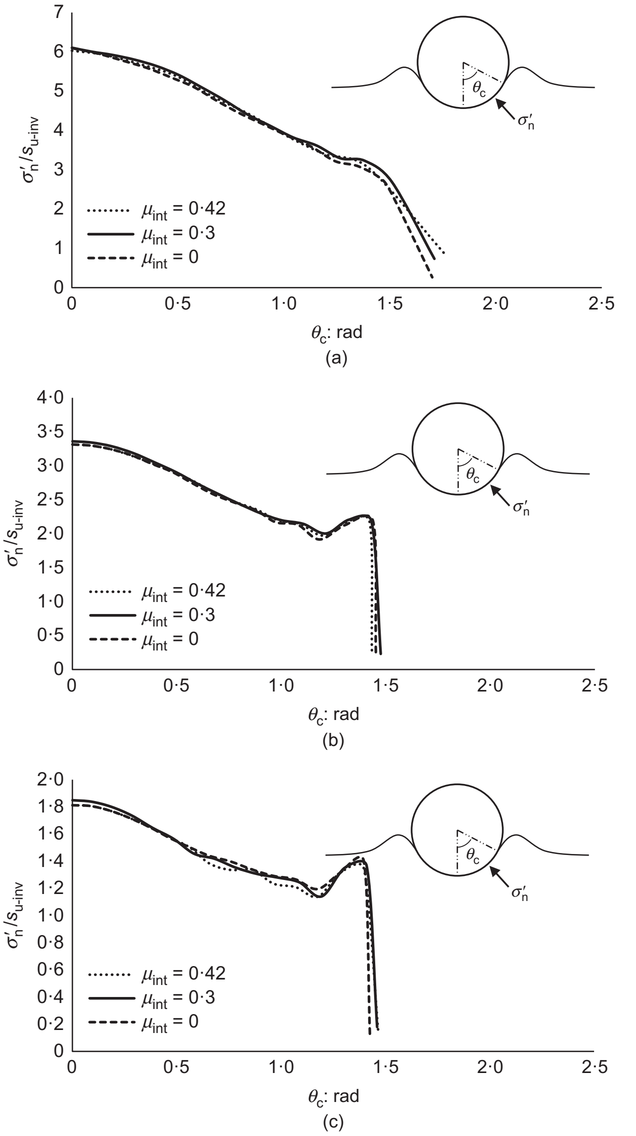

Fig. 22. The normal contact stresses around the pipe after penetration-induced excess pore pressure dissipation – that is, drained condition – for different interface friction coefficient μ_{int} and VLR (for $M = 0{\cdot}9$, $\lambda = 0{\cdot}25$, and $\kappa = 0{\cdot}05$) at embedment depth of $0{\cdot}5D_{\text{p}}$: (a) VLR = 1; (b) VLR = 0·5; (c) VLR = 0·25

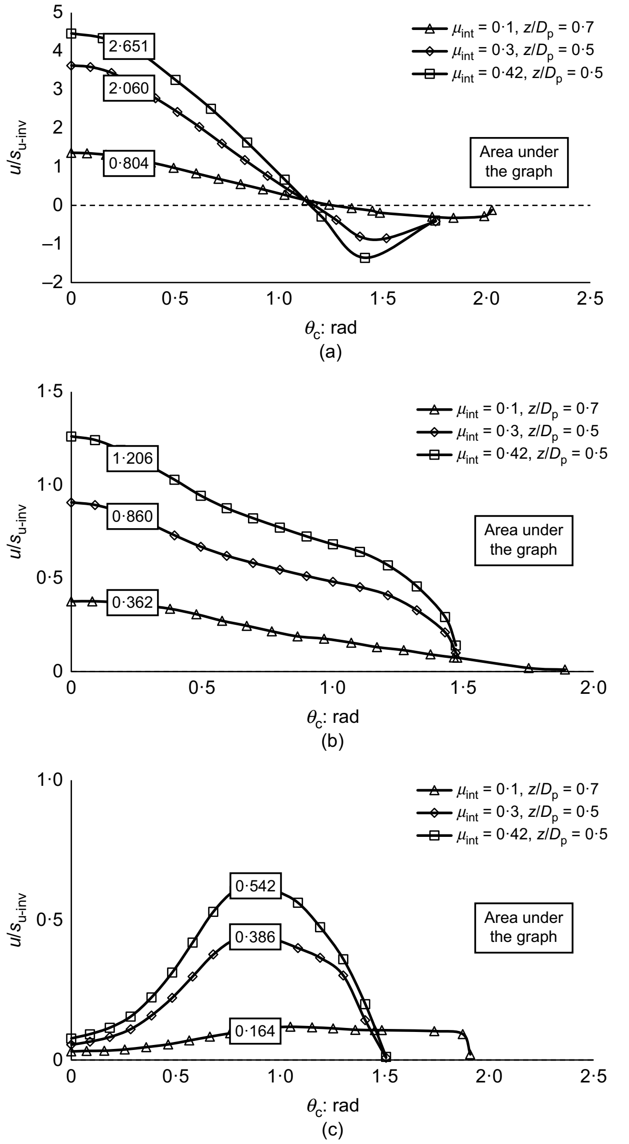

Fig. 23. Shear-induced excess pore pressure around the pipe during fast axial sliding – that is, undrained condition – for different interface friction coefficients μ_{int} and VLRs (for $M = 0{\cdot}9$, $\lambda = 0{\cdot}25$, and $\kappa = 0{\cdot}05$): (a) VLR = 1; (b) VLR = 0·5; (c) VLR = 0·25

(see Fig. 23). This can be attributed to the fact that higher interface friction mobilises higher shear stresses in the soil, thereby raising the excess pore pressure. As Fig. 24 shows, the effect of interface friction coefficient on the integrated interface excess pore pressure U can be described approximately by

$$U = C\mu_{\text{int}}\left(\frac{z}{D_{\text{p}}}\right)^{0{\cdot}7} R^{1{\cdot}15} \tag{17}$$

with $C = 10{\cdot}3$. This allows equation (16) to be re-expressed as

$$\zeta_{\text{u}} = \zeta_{\text{d}} - \frac{10{\cdot}3\mu_{\text{int}} s_{\text{u-inv}} z^{0{\cdot}7} D_{\text{p}}^{0{\cdot}3} R^{1{\cdot}15}}{V'} \tag{18}$$

For an enhancement factor pertaining to intermediate sliding velocity, a relative enhancement index Ψ can be defined herein by

$$\Psi = \frac{\zeta - \zeta_{\text{u}}}{\zeta_{\text{d}} - \zeta_{\text{u}}} \tag{19}$$

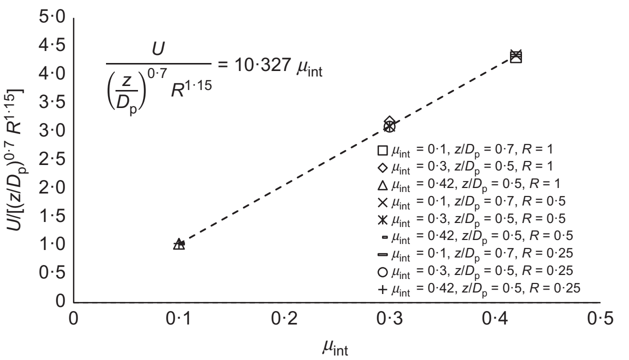

Fig. 24. Effect of interface friction coefficient on the integrated interface shear-induced excess pore pressure – that is, $U/(z/D_{\text{p}})^{0{\cdot}7}R^{1{\cdot}15}$ – plotted against μ_{int}

where ζ is the enhancement factor corresponding to intermediate sliding velocities. As Fig. 25 shows, for a given VLR, the computed results are narrowly bounded and can be

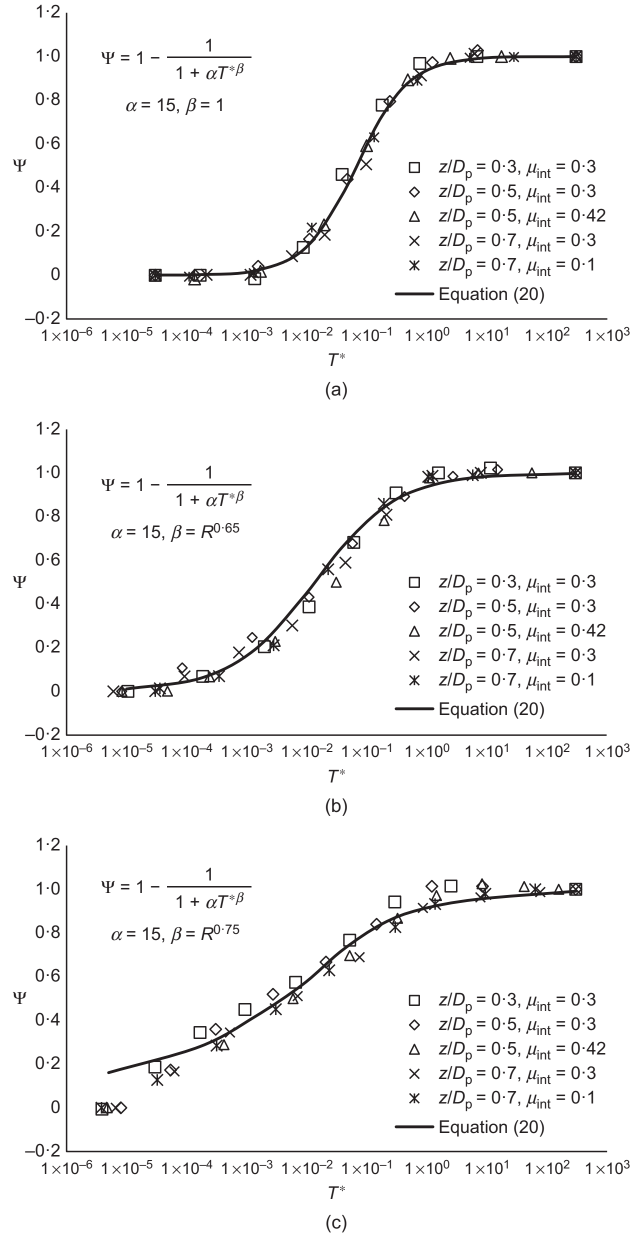

Fig. 25. Relative enhancement index Ψ for intermediate sliding velocity: (a) VLR = 1; (b) VLR = 0·5; (c) VLR = 0·25

described by an equation of the form

$$\Psi = 1 - \frac{1}{1 + \alpha T^{*\beta}} \tag{20}$$

where α and β are fitted parameters; $\alpha = 15$ and $\beta \sim R^{0{\cdot}68} - R^{0{\cdot}75}$. The relative enhancement index Ψ of 0 and 1 corresponds to undrained and fully drained conditions, respectively.

CONCLUSION

There are two elements of novelty in this study. First, a 3D RITSS coupled effective stress finite-element study using the Cam Clay model was employed to investigate axial pipe–soil interaction behaviour. The analysis procedure utilises the Abaqus mesh-to-mesh solution mapping feature, fully automated through a Python script without any user intervention. The mapping of the updated yield surface size was achieved by coding the Cam Clay model as a user-defined material subroutine. Previous studies involving RITSS and the Cam Clay model were limited to two-dimensional analyses, which were unable to model pipe embedment with follow-on sliding.

The current study highlighted the influence of some of the factors affecting the post-laying consolidation and axial sliding processes of as-laid pipelines. First, the effect of soil properties on the effective normal contact stress and excess pore pressure can be largely accounted for by normalising these quantities by the in situ undrained shear strength at the invert. The interface friction coefficient also does not have a significant influence on the post-laying excess pore pressure and post-consolidation effective normal contact stress. However, the sliding-induced excess pore pressure increases significantly with interface friction coefficient.

The two parameters that were found to exercise the strongest influence on the post-consolidation and sliding behaviour of the pipeline were the embedment ratio and vertical load ratio. This recognition allows the embedment enhancement factor for very slow sliding, corresponding to effectively drained conditions, to be adequately reflected by empirically fitted relationships involving the embedment and vertical load ratios. For very fast sliding, corresponding to effectively undrained conditions, an empirically fitted relationship involving embedment and vertical load ratios and interface friction coefficients is also proposed. Finally, the variation of embedment enhancement factor with sliding velocity can also be expressed in terms of a relative enhancement index, which can be adequately described by hyperbolic relationships. Together, these relationships allow axial sliding resistance corresponding to any sliding velocity to be assessed; this is expected to be of use in the design of as-laid underwater pipelines in soft clayey soils. This constitutes the second element of novelty.

The results presented above are based on tests and computations for normally consolidated clays, which generate positive excess pore pressures under undrained shearing. They may not be applicable to stiff, highly overconsolidated clays, which may generate negative excess pore pressures during undrained shearing.

ACKNOWLEDGEMENTS

The authors acknowledge the research funding provided by the Singapore Maritime Institute and the American Bureau of Shipping for the project entitled ‘Pipeline–soil–water interaction effects for realistic deep-water pipeline design’ under the Deepwater Technology R&D Programme. The first author also acknowledges the funding provided by the National University of Singapore research scholarship.

NOTATION

A	dimensionless time at which ξ has decreased to half of its initial value
c_v	coefficient of consolidation
D_p	pipe diameter
e_0	initial void ratio
e_N	void ratio of virgin compression line at $p' = 1$ kPa
F	axial sliding resistance
F_d	drained axial sliding resistance
F_u	undrained axial sliding resistance
K_0	lateral earth pressure coefficient at rest
k	permeability of soil
M	slope of critical state line
m	fitted index for lay-induced and sliding-induced excess pore pressure
m_v	coefficient of volume change
p'	mean effective stress
R	vertical load ratio

S integral of normalised effective contact stress
S_0 integral of normalised effective contact stress for VLR of 1
s_u undrained shear strength
$s_{u\text{-inv}}$ undrained shear strength at the pipe invert
T^* dimensionless time from the initiation of axial sliding
T_L dimensionless time after pipe penetration
T_L^p dimensionless time to peak lay-induced excess pore pressure
T_p^* dimensionless time to peak sliding-induced excess pore pressure
t elapsed time after pipe penetration
t^* elapsed time from the initiation of axial sliding
U integral of normalised excess pore pressure
U_0 integral of normalised excess pore pressure for VLR of 1
u excess pore pressure
V net penetration resistance per unit length
V' submerged pipe weight per unit length
V_s dimensionless axial sliding velocity
v_s axial sliding velocity
X fitted index for peak sliding-induced excess pore pressure
z depth of embedment
α fitted parameter for relative enhancement index
β fitted parameter for relative enhancement index
γ_w unit weight of water
ζ enhancement factor
ζ_d drained enhancement factor
ζ_u undrained enhancement factor
κ slope of unloading/reloading line
λ slope of normal compression line
μ_{int} pipe–soil interface friction coefficient
ξ normalised excess pore pressure
ξ_0 initial normalised excess pore pressure
σ_n' effective normal contact stress
σ_v' vertical effective stress
Ψ relative enhancement index

REFERENCES

Abaqus (2016). *ABAQUS Analysis user's guide, version 2016*. Johnston, RI, USA: Dassault Systemes Simulia Corp.

Ansari, Y., Kouretzis, G. P. & Sheng, D. (2014). An effective stress analysis of partially embedded offshore pipelines: vertical penetration and axial walking. *Comput. Geotech.* **58**, 69–80, https://doi.org/10.1016/j.compgeo.2014.01.011.

Ballard, J. C., van den Abeele, F. & Brier, C. (2013). Influence of axial response on pipeline end expansion and walking. *6th International pipeline technology conference*, Ostend, Belgium, paper S30-01.

Boukpeti, N. & White, D. J. (2017). Interface shear box tests for assessing axial pipe-soil resistance. *Géotechnique* **67**, No. 1, 18–30, https://doi.org/10.1680/jgeot.15.P.112.

Bruton, D. A. S., Bolton, M., Carr, M. & White, D. (2008). Pipe-soil interaction With flowlines during lateral buckling and pipeline walking – the SAFEBUCK JIP. *Proceedings of the offshore technology conference*, Houston, TX, USA, paper OTC-19589-MS, https://doi.org/10.4043/19589-MS.

BSI (1993). BS 8010-3: Code of practice for pipelines Part 3: Pipelines subsea: design, construction and installation. London, UK: BSI.

Carr, M., Sinclair, F. & Bruton, D. (2008). Pipeline walking – understanding the field layout challenges and analytical solutions developed for the Safebuck JIP. *SPE Projects, Facilities Constr.* **3**, No. 3, 1–9, https://doi.org/10.2118/120022-PA.

Carter, J. P. & Balaam, N. P. (1995). *AFENA User manual 5.0*. Sydney, Australia: Geotechnical Research Centre, University of Sydney.

Chang, M. F., Teh, C. I. & Cao, L. (1999). Critical state strength parameters of saturated clays from the modified cam-clay model. *Can. Geotech. J.* **36**, No. 5, 876–890, https://doi.org/10.1139/t99-050.

Chung, S. F., Randolph, M. F. & Schneider, J. A. (2006). Effect of penetration rate on penetrometer resistance in clay. *J. Geotech. Geoenviron. Engng* **132**, No. 9, 1188–1196, https://doi.org/10.1061/(ASCE)1090-0241(2006)132:9(1188).

DNV GL (Det Norske Veritas Germanischer Lloyd) (2017). *RP-F114: pipe–soil interaction for submarine pipelines.* Oslo, Norway: DNV GL.

Dutta, S., Hawlader, B. & Phillips, R. (2015). Finite element modeling of partially embedded pipelines in clay seabed using coupled Eulerian–Lagrangian method. *Can. Geotech. J.* **52**, No. 1, 58–72, https://doi.org/10.1139/cgj-2014-0045.

Finnie, I. M. S. & Randolph, M. F. (1994). Punch-through and liquefication induced failure of shallow foundations on calcareous sediments. In *International conference on behaviour of offshore structures – BOSS'94. Vol. 1: geotechnics* (ed. C. Chryssostomidis), pp. 217–230. Oxford, UK: Pergamon.

Goh, T. L. (2003). *Stabilization of an excavation by an embedded improved soil layer.* PhD thesis, National University of Singapore, Singapore.

Hossain, M. S., Randolph, M. F., Hu, Y. & White, D. J. (2006). Cavity stability and bearing capacity of spudcan foundations on clay. *Proceedings of the offshore technology conference*, Houston, TX, USA, paper OTC-17770-MS, https://doi.org/10.4043/17770-MS.

Hu, Y. & Randolph, M. F. (1998a). A practical numerical approach for large deformation problems in soil. *Int. J. Numer. Analyt. Methods Geomech.* **22**, No. 5, 327–350, https://doi.org/10.1002/(SICI)1096-9853(199805)22:5<327::AID-NAG920>3.0.CO;2-X.

Hu, Y. & Randolph, M. F. (1998b). H-adaptive FE analysis of elasto-plastic non-homogeneous soil with large deformation. *Comput. Geotech.* **23**, No. 1, 61–83, https://doi.org/10.1016/S0266-352X(98)00012-3.

Huang, J. & Griffiths, D. V. (2009). Return mapping algorithms and stress predictors for failure analysis in geomechanics. *J. Engng Mech.* **135**, No. 4, 276–284, https://doi.org/10.1061/(ASCE)0733-9399(2009)135:4(276).

Krost, K., Gourvenec, S. M. & White, D. J. (2011). Consolidation around partially embedded seabed pipelines. *Géotechnique* **61**, No. 2, 167–173, https://doi.org/10.1680/geot.8.T.015.

Li, Y. P., Yi, J. T., Lee, F. H., Goh, S. H., Liu, Y., Yang, Y., Zhang, X. Y. & Wu, J. F. (2017). Effects of the lattice leg on cavities and bearing capacity of deeply embedded spudcans in clay. *Géotechnique* **67**, No. 1, 1–17, https://doi.org/10.1680/jgeot.15.P.014.

Palmer, A. (2008). Touchdown indentation of the seabed. *Appl. Ocean Res.* **30**, No. 3, 235–238, https://doi.org/10.1016/j.apor.2008.09.004.

Randolph, M. F. & Hope, S. (2004). Effect of cone velocity on cone resistance and excess pore pressures. In *Proceedings of the IS Osaka – engineering practice and performance of soft deposits* (eds T. Matsui, Y. Tanaka and M. Mimura), pp. 147–152. Osaka, Japan: Yodogawa Kogisha Co. Ltd.

Randolph, M. F. & White, D. (2008). Pipeline embedment in deep water: processes and quantitative assessment. *Proceedings of the offshore technology conference*, Houston, TX, USA, paper OTC-19128-MS, https://doi.org/10.4043/OTC-19128-MS.

Randolph, M. F., White, D. J. & Yan, Y. (2012). Modelling the axial soil resistance on deep-water pipelines. *Géotechnique* **62**, No. 9, 837–846, https://doi.org/10.1680/geot.12.OG.010.

Satchithananthan, U., Ullah, S. N., Lee, F. H., Chen, Z. & Gu, H. (2019). Centrifuge modeling of axial pipe–soil interaction of deep-water pipelines. *Geotech. Test. J.* **43**, No. 1, 94–112, https://doi.org/10.1520/GTJ20180229.

Tian, Y., Cassidy, M. J., Randolph, M. F., Wang, D. & Gaudin, C. (2014). A simple implementation of RITSS and its application in large deformation analysis. *Comput. Geotech.* **56**, 160–167, https://doi.org/10.1016/j.compgeo.2013.12.001.

Ullah, S. N., Lee, F. H., Satchithananthan, U., Chen, Z. & Gu, H. (2018). A 3D RITSS approach for total stress and coupled-flow large deformation problems using ABAQUS. *Comput. Geotech.* **99**, 203–215, https://doi.org/10.1016/j.compgeo.2018.01.018.

Wang, D., Randolph, M. F. & White, D. J. (2010). Large-deformation finite element analysis of pipe penetration and large-amplitude lateral displacement. *Can. Geotech. J.* **47**, No. 8, 842–856, https://doi.org/10.1139/T09-147.

Westgate, Z. J., White, D. J. & Randolph, M. F. (2012). Modelling the embedment process during offshore pipe-laying on fine-grained soils. *Can. Geotech. J.* **50**, No. 1, 15–27, https://doi.org/10.1139/cgj-2012-0185.

White, D. J. & Randolph, M. F. (2007). Seabed characterisation and models for pipeline–soil interaction. *Int. J. Offshore Polar Engng* **17**, No. 03, 12.

White, D. J., Gaudin, C., Boylan, N. & Zhou, H. (2010). Interpretation of T-bar penetrometer tests at shallow embedment and in very soft soils. *Can. Geotech. J.* **47**, No. 2, 218–229, https://doi.org/10.1139/T09-096.

Yan, Y., Randolph, M. F. & White, D. J. (2017). Elastoplastic consolidation solutions for scaling from shallow penetrometers to pipelines. *Can. Geotech. J.* **54**, No. 6, 881–895, https://doi.org/10.1139/cgj-2016-0286.

Yi, J. T., Zhao, B., Li, Y. P., Yang, Y., Lee, F. H., Goh, S. H., Zhang, X. Y. & Wu, J. F. (2014). Post-installation pore-pressure changes around spudcan and long-term spudcan behaviour in soft clay. *Comput. Geotech.* **56**, 133–147, https://doi.org/10.1016/j.compgeo.2013.11.007.